



ACADÉMIE  
DES SCIENCES  
INSTITUT DE FRANCE

# *Comptes Rendus*

---

## *Physique*

Peter Read, Yakov Afanasyev, Jonathan Aurnou and Daphné Lemasquerier


### **Eddy-driven Zonal Jet Flows in the Laboratory**

Published online: 20 December 2024

**Part of Special Issue:** Geophysical and astrophysical fluid dynamics in the laboratory

**Guest editors:** Stephan Fauve (Laboratoire de Physique de l'ENS, CNRS, PSL Research University, Sorbonne Université, Université Paris Cité, Paris, France) and Michael Le Bars (CNRS, Aix Marseille Univ, Centrale Marseille, IRPHE, Marseille, France)

<https://doi.org/10.5802/crphys.213>

 This article is licensed under the  
CREATIVE COMMONS ATTRIBUTION 4.0 INTERNATIONAL LICENSE.  
<http://creativecommons.org/licenses/by/4.0/>



*The Comptes Rendus. Physique are a member of the  
Mersenne Center for open scientific publishing*  
[www.centre-mersenne.org](http://www.centre-mersenne.org) — e-ISSN : 1878-1535



Review article / *Article de synthèse*

Geophysical and astrophysical fluid dynamics in the laboratory /  
*Dynamique des fluides géophysiques et astrophysiques au  
laboratoire*

# Eddy-driven Zonal Jet Flows in the Laboratory

## *Jets zonaux en expériences de laboratoire*

Peter Read <sup>\*,a</sup>, Yakov Afanasyev <sup>b</sup>, Jonathan Aurnou <sup>c</sup> and Daphné Lemasquerier <sup>d</sup>

<sup>a</sup> Department of Physics, University of Oxford, UK

<sup>b</sup> Department of Physics and Physical Oceanography, Memorial University of Newfoundland, Canada

<sup>c</sup> Department of Earth, Planetary and Space Sciences, University of California, Los Angeles, USA

<sup>d</sup> School of Mathematics and Statistics, University of St Andrews, UK

*E-mails:* peter.read@physics.ox.ac.uk (P. Read), afanai@mun.ca (Y. Afanasyev), jona@epss.ucla.edu (J. Aurnou), d.lemasquerier@st-andrews.ac.uk (D. Lemasquerier)

**Abstract.** Zonal jets are a ubiquitous feature of the circulation of planetary atmospheres, oceans and interiors. Many of the dynamical mechanisms that lead to the formation and evolution of such jets can be reproduced and studied in laboratory experiments, which have proved to be important sources of insight for understanding the nature of planetary jets. Here we introduce some of the key concepts underlying the production and maintenance of patterns of zonal jets in rotating and/or stratified flows. We then review a broad range of laboratory experiments that have helped to test and verify many of the dynamical mechanisms proposed to interpret geophysical jets involving the interaction of eddies and zonal flows. Laboratory experiments continue to have an important role to play in elucidating a quantitative understanding of zonal jets and their interactions with other aspects of planetary circulation systems.

**Résumé.** Les courants ou jets zonaux sont des éléments clés de la dynamique des enveloppes fluides planétaires, depuis les atmosphères et océans jusqu'aux intérieurs liquides profonds. Les expériences de laboratoire permettent de reproduire plusieurs mécanismes à l'origine des jets zonaux dans un environnement contrôlé, et ont ainsi joué un rôle déterminant dans notre compréhension de la physique des jets. Après avoir introduit les concepts fondamentaux à l'émergence et la persistance de jets zonaux dans des écoulements tournants et/ou stratifiés, nous faisons une synthèse des dispositifs expérimentaux ayant permis de tester ou valider certains mécanismes à l'origine des jets dans les écoulements géophysiques, en particulier du point de vue des interactions entre fluctuations (ondes, tourbillons) et écoulement moyen (jets). Les expériences de mécanique des fluides ont un rôle central à jouer afin de tendre vers une compréhension quantitative de la dynamique jets zonaux au sein des systèmes fluides planétaires, et de leur interaction avec les autres composantes de la circulation.

**Keywords.** jets, eddies, Reynolds stress, wave-zonal flow interaction, Rossby waves.

**Mots-clés.** jets, tourbillons, tensions de Reynolds, interaction onde-écoulement zonal, ondes de Rossby.

\*Corresponding author

**Funding.** JA thanks the NSF Geophysics Program for support via award EAR #2143939. DL acknowledges support from The Carnegie Trust via Research Incentive Grant RIG012674, and the Royal Society via Research Grant RG/R1/241426. YA is supported by the NSERC grant RGPIN 2019-04957 and PLR acknowledges support from UKRI/EPSC grant EP/W022087/1.

*Manuscript received 17 May 2024, revised and accepted 3 October 2024.*

## 1. Introduction

Jet streams and other intense currents are common features of the circulation of planetary atmospheres, oceans and other geophysical contexts. Such jet-like flows in rotating and/or homogeneous or stratified fluids are phenomena that are well suited for demonstration and quantitative investigation in fluid dynamics laboratories. The topic has a long and distinguished history going back more than 60 years, and a variety of different experimental approaches and dynamical mechanisms have been studied, ranging from directly forced jets, using mechanical or buoyancy forcing, to complex eddy-driven zonal flows. Here we focus on the latter as representing the most interesting and challenging to understand.

As noted by Rhines [1], “it is not easy to give a precise definition of a jet of fluid motion, but most of us know one when we see it”. Such a statement is clearly unsatisfactory from a theoretical standpoint but the concept of a jet can be applied to a variety of phenomena where flows are elongated along a particular direction and are energetic and persistent in time. For the present purpose, we adopt a set of criteria for jet-like flows that largely follows that of [2]. These criteria can be summarised as characterising a flow with the following properties:

- (1) *Anisotropy* – length scale along the direction of the current is much longer than the width of the current;
- (2) *Transport* – fluid near the centre of the current is transported along the current a distance much larger than the current width;
- (3) *Connectivity* – the separation distance in the direction of the jet of nearby fluid elements near the centre of the jet diverges only slowly;
- (4) *Longevity* – the jet pattern persists much longer than the advective timescale.

Zonal flows wrap around a system’s rotation axis, traditionally oriented in  $\hat{z}$ . Thus, they are oriented in the azimuthal  $\hat{\phi}$ -direction in spherical  $(r, \theta, \phi)$  or cylindrical  $(s, z, \phi)$  coordinate systems. These flows travel along lines of latitude in planetary fluid layers. Geophysical zonal jets are relatively thin, coherent, azimuthal flows that form latitudinal stripes painted across the face, and potentially interior, of a given planetary body. Famous examples include zonal winds in the atmospheres of Earth and Jupiter and zonal currents such as the Antarctic Circumpolar Current in Earth’s Southern Ocean. For a comprehensive description of zonal jets in nature, the reader is referred to [3, Part II].

The ability to capture such phenomena under conditions and on scales that share significant dynamical similarity with those of large-scale systems in geophysics and astrophysics is potentially powerful, though should not be taken for granted. As discussed in the next section, it follows for rapidly rotating fluids from the dominance of the geostrophic balance in the horizontal momentum equations, in which Coriolis accelerations are balanced mainly by specific pressure gradient forces and other effects, such as due to viscous dissipation or inertial accelerations, are relatively much weaker. This allows the detailed investigation and measurement of geophysically and astrophysically relevant dynamical processes in well controlled and repeatable experiments that are not subject to limitations and uncertainties associated either with simplifying approximations, necessary for progress in analytical and numerical models, or incomplete and sparse observations and lack of repeatability when measuring flow systems in nature.

Of course, laboratory investigations are subject to other kinds of limitation, associated e.g. with the practical requirements to impose boundary conditions or geometrical constraints that have no counterpart in geophysics or astrophysics, or the use of viscous, thermally-conducting liquids in place of nearly inviscid gases or plasmas. But the ability to produce and study fully developed and highly nonlinear flows *in real fluids* under controlled conditions provides opportunities to gain insights that strongly complement other approaches based on mathematical analysis, numerical simulation or direct observations of natural systems.

Here we focus on some key questions that relate to our general understanding of zonal jets and their occurrence and behaviour in geophysical and astrophysical contexts. In particular, we consider the following specific questions and the ways in which laboratory experiments have offered in the past, and continue to offer, useful insights into the processes that create and maintain zonal jets in the atmospheres, oceans and interiors of planetary bodies.

- How are jets driven by eddies and waves?
- What determines the amplitude of the rectified flow?
- What determines the shape and width of the induced jets?
- What is the nature of the scale to scale interactions that produce jets?

Section 2 introduces some of the basic scales and parameters that are relevant to determining the origin and properties of zonal jets, and which link phenomena on laboratory and geophysical scales. Section 3 reviews the basic theory underlying the formation of zonal flows by the action of nonlinear eddies that is useful when interpreting experimental results, while Section 4 outlines some of the main experimental techniques used to investigate jet formation phenomena in the laboratory. Sections 5 and 6 review a wide range of experiments and results on zonal jet formation, distinguishing between forcings that are either localised or global in space. Finally, some concluding remarks are presented in Section 7.

## 2. Basic parameters, scales and flow regimes

One of the most fundamental pre-requisites for laboratory experiments to provide insights which may be useful in the context of large-scale geophysical or astrophysical circulations is that of *dynamical similarity*. This essentially determines whether laboratory flows may serve as analogues of large-scale geophysical or astrophysical flow systems and have the same primary balance of forces acting as in their atmospheric or oceanic counterparts. This is generally verified by various forms of *Scale analysis*. Ideally, also, there should be some similarity of boundary conditions, at least in so far as they affect the way in which motions are driven and/or contained within both systems.

### 2.1. Scales and dimensionless parameters

The main balances and dominant terms in the governing equations are typically estimated with reference to sets of dimensionless parameters which are commonly designed to indicate the ratios of terms in those governing equations or ratios of characteristic length or timescales. Table 1 summarizes the dimensionless numbers discussed throughout this review, along with their definitions, while Table 2 provides estimates of many of these parameters for both natural flows and laboratory experiments, as discussed in Section 2.4. In Table 1 and elsewhere,  $U$  is a typical (horizontal) velocity,  $\Omega$  is the angular velocity of the rotating frame and  $f_0 = 2\Omega \sin \phi_0$  the Coriolis parameter at reference latitude  $\phi_0$ ,  $\mathbf{g}$  the acceleration due to gravity,  $\Delta_{\rho(v,h)} = \Delta\rho/\rho$  the fractional density perturbation (in the Boussinesq approximation), where  $\rho$  is density,  $\nu$  is the kinematic viscosity and  $\kappa$  the thermal diffusivity [4]. The subscript  $\nu$  or  $h$  in  $\Delta_{\rho(v,h)}$  represents

the fractional density perturbation in either the vertical or horizontal respectively. The strength of the stratification is measured by the buoyancy frequency  $N$ , typically defined by

$$N^2 = -g \frac{\partial \ln \rho}{\partial z}. \quad (1)$$

From these physical parameters, several dimensionless parameters can be introduced to characterize the dynamical regimes of planetary flows [4] and the extent to which dynamical similarity can be obtained experimentally (Section 2.4). The importance of the Coriolis acceleration relatively to inertial forces in the Navier–Stokes equations is represented by the Rossby number  $Ro$ . When  $Ro \ll 1$ , the flow is strongly affected by rotation. The relative strength of viscous forces to Coriolis accelerations is measured by the Ekman number.  $E \ll 1$  for sufficiently rapidly rotating systems and is related to the Rossby number by  $Ro = E \times Re$ , where  $Re$  is the Reynolds number measuring the relative strength of inertial to viscous forces ( $Re \gg 1$  for turbulent flows).

The Burger number  $Bu$  measures the relative strength of stratification to rotation effects. It is approximately equivalent to the inverse of the Rotational Froude number), which is typically  $O(1)$  for energetically favoured scales of motion in a stably-stratified, rotating flow. For thermally-driven flows, we introduce the Rayleigh number  $Ra$ , an important parameter in many convection problems, which measures the relative importance of buoyancy forces to the effects of viscous and thermal diffusion, and the Prandtl number which compares viscous to thermal diffusion. The Rayleigh number is sometimes more conveniently defined with respect to the buoyancy flux,  $F_B$ , as the Flux Rayleigh number  $Ra_F$ , where  $F_B$  is defined with respect to the heat flux  $F_H$  as

$$F_B = \frac{g \Delta \rho_{(v,h)} F_H}{\rho c_p}, \quad (2)$$

where  $c_p$  is the specific heat capacity.

## 2.2. $\beta$ -effects in planetary settings and in the laboratory

A further factor which sometimes leads to misconceptions regarding the extent to which dynamical similarity between laboratory flows and atmospheric or oceanic circulations can be achieved concerns the  $\beta$ -effect of dynamical meteorology and oceanography. This is traditionally interpreted as the effect of the spherical curvature of the planet on Coriolis forces, though actually manifests itself in the balance of vorticity transport. In the former interpretation (often cited by

**Table 1.** Definition of the dimensionless parameters provided in Table 2.  $L$  and  $D$  are typical horizontal and vertical length scales, respectively.

|           | Definition  | Expression  |
|-----------|---|---|
| $\eta$    | Vertical/Horizontal aspect ratio                                | $D/L$   |
| $Ro$      | Rossby number (inertia/Coriolis)                                | $U/(f_0 L)$   |
| $E$       | Ekman number (viscous effects/Coriolis)                         | $\nu/(f_0 D^2)$   |
| $Re$      | Reynolds number (inertia/viscous effects)                       | $UL/\nu$  |
| $Bu$      | Burger number (stratification/rotation)                         | $(ND/(f_0 L))^2$  |
| $Ra$      | Rayleigh number (buoyancy/diffusion)                            | $g \Delta \rho_{(v)} D^3 / (\kappa \nu)$<br>or $g \Delta \rho_{(h)} L^3 / (\kappa \nu)$ |
| $Ra_F$    | Flux Rayleigh number (buoyancy/diffusion)                       | $F_B D^4 / (\nu^2 \kappa)$  |
| $Pr$      | Prandtl number (viscous/thermal diffusivity)                    | $\nu/\kappa$  |
| $\beta_1$ | $\beta$ -planarity (linearity of planetary vorticity gradients) | $\beta L / f_0$   |
| $\beta_2$ | planetary vorticity/relative vorticity gradients                | $\beta L^2 / U$   |
| $R_\beta$ | Zonostrophy (Rhines/transitional scales)                        | $(\beta U^5 / \epsilon^2)^{1/10}$   |

meteorologists and oceanographers), the Coriolis parameter  $f$  is considered to be the projection of the planetary angular velocity vector onto the local vertical, so that

$$f = 2\Omega \sin \phi \quad (3)$$

where  $\phi$  is the latitude. The  $\beta$  term then represents the latitudinal gradient of  $f$ :

$$\beta = \frac{1}{R} \frac{\partial f}{\partial \phi} = \frac{2\Omega \cos \phi}{R}, \quad (4)$$

where  $R$  is the radius of the planet. More generally, however, the  $\beta$ -effect may be regarded as resulting from the conservation of a barotropic *Potential vorticity*

$$q = \frac{(2\Omega + \zeta)}{h}, \quad (5)$$

where  $\zeta$  and  $h$  are respectively the components of relative axial vorticity and distance between the upper and lower boundaries along the rotation axis  $\Omega \hat{\mathbf{z}}$ . For the case of a *very thin* spherical shell of uniform thickness  $D \ll R$ ,

$$h \simeq \frac{D}{\sin \phi} \quad (6)$$

inside the tangent cylinder (i.e. the cylinder just enclosing the inner sphere [5–7]), and the “planetary vorticity” component of  $q$  in (5) takes the form  $q \simeq (2\Omega \sin \phi)/D$ , thereby emulating the dependence of  $f$  on latitude commonly assumed in terrestrial meteorology.

Space missions have revealed the existence of deep zonal jets on the gas planets, in which the depth of the zonal jet flows can extend thousands of kilometers below the planet’s observable surface [8–10]. Subsurface oceans have been detected as well within our solar system’s icy moons [11, 12], and may reasonably harbor strong deep jet flows [13, 14]. These subsurface oceans may be 100’s of kilometer deep on planets with radii far smaller than that of Earth. In these layers, the traditional shallow layer  $\beta$  formulation, which applies accurately to Earth’s ocean and to planetary tropospheric layers, becomes progressively less accurate (with a fractional error  $O(D/2R)$ ) as  $D/R$  increases and/or the tangent cylinder latitude is approached. In this case, it is best to consider  $\beta_T$ , the topographic  $\beta$  formulation,

$$\beta_T = \frac{2\Omega}{h} \frac{\partial h}{\partial s}, \quad (7)$$

where  $s$  denotes cylindrical radius (from the rotation axis) and it is assumed that axial fluid layer height variations  $h$  arise only due to the shape of the axisymmetric, spherical shell boundaries (e.g., [15, 16]). Non-axisymmetric topographic features are not considered (cf. [17–20]).

The  $\beta_T$  approach leads to different formulations for a thick shell especially close to the equator outside the tangent cylinder (e.g. see [16, 21]). Such a topographic  $\beta$ -effect is thus equivalent to the meteorological “planetary vorticity gradient” for barotropic flows, and also for two-layer baroclinic flows where the lower *and upper* boundaries slope in equal and opposite senses. For more general rotating, stratified flows, however, the  $\beta$ -effect associated with topographic slopes is no longer formally equivalent to the “planetary vorticity gradient” in a spherical shell, though it is empirically observed to lead to *qualitatively* similar effects (Rossby-like wave dispersion etc. – e.g. see [22]).

The vast majority of laboratory zonal jets experiments are carried out in geometrically thick fluid layers in which  $D$  is not orders of magnitude less than  $L$ . This is because it is difficult in laboratory settings to generate extremely thin fluid layers that are strongly turbulent and strongly influenced by rotation (cf. [23]). Thus, the topographic  $\beta$  approach is employed ubiquitously in laboratory jets studies (e.g., [15, 24]). The essential effect of  $\beta$  is to describe how the planetary vorticity varies spatially, regardless of formulation.

Two dimensionless terms can be defined involving  $\beta$ ,

$$\beta_1 \sim \frac{\beta L}{f} \quad (8)$$

and

$$\beta_2 \sim \frac{\beta L^2}{U}. \quad (9)$$

If  $\beta_1$  is much less than unity, then  $f$  effectively changes little across the domain of interest, suggesting that the full spherical geometry can be replaced (at least conceptually) by a tangent plane centred at a particular latitude  $\phi_0$  such that  $f = f_0 + \beta y$ , where  $f_0 = 2\Omega \sin \phi_0$  and  $y$  is a Cartesian lateral coordinate. The parameter  $\beta_2$ , on the other hand, represents a ratio of “planetary vorticity gradient” (denoted by  $\beta$  itself) to that of relative vorticity ( $\sim U/L^2$ ), and provides a measure of the relative importance of planetary vorticity gradients in the dynamics to that of relative vorticity advection.

In experiments with a free surface and fast rotation, one can take an advantage of the parabolic shape of the surface when in solid-body rotation. The depth of the fluid layer in a cylindrical tank of radius  $R$  is given by

$$h(s) = H + \frac{\Omega^2}{2g} \left( s^2 - \frac{R^2}{2} \right), \quad (10)$$

where  $s$  is the distance from the axis of rotation as before,  $H$  is the depth of the layer in the absence of rotation,  $\Omega$  is the rotation rate of the tank and  $g$  is the gravitational acceleration. Using the background potential vorticity (PV),  $q = 2\Omega/h$ , one can show that the quadratic depth variation is dynamically equivalent to the Coriolis parameter varying quadratically with radius,  $f = 2\Omega - \gamma s^2$  where  $\gamma = \Omega^3/(gH)$ . The laboratory flows can be related to those on a rotating planet where

$$f = 2\Omega \cos \varphi \approx 2\Omega \left( 1 - \frac{\varphi^2}{2} \right) = 2\Omega - \frac{\Omega}{R^2} r_s^2. \quad (11)$$

Here  $\varphi$  is the colatitude,  $R$  is the radius of the planet, and  $r_s$  is the spherical distance from the pole. This approximation is called the polar beta-plane or, alternatively, the gamma-plane. It is well suited for regional domains which include the pole.

### 2.3. Zonostrophic and friction-dominated regimes

In the context of eddy-driven zonal jets in forced-dissipative flows, the formation of strong, well delineated jets is a particular characteristic of the “zonostrophic” regime [25, 26]. This regime is defined in terms of the ratio of scales between the Rhines scale, or Rhines wavenumber

$$k_R = \left( \frac{\beta}{U} \right)^{1/2}, \quad (12)$$

(where  $U$  is usually taken to imply the rms eddy velocity scale) and the eddy anisotropy scale, or eddy anisotropy wavenumber

$$k_\beta = \left( \frac{\beta^3}{\epsilon} \right)^{1/5}, \quad (13)$$

where  $\epsilon$  represents the rate of upscale energy transfer within the turbulent energy cascade. The Rhines scale ( $\propto k_R^{-1}$ ) estimates the halting scale at beyond which jets and eddies cease to grow on the  $\beta$ -plane [27, 28]. The eddy anisotropy scale ( $\propto k_\beta^{-1}$ ) defines the scale at which the eddy overturning timescale is equal to that due to Rossby wave propagation and represents the scale at

which the character of the flow changes from being roughly isotropic (at smaller scales) to being highly anisotropic (at larger scales) [25]. The ratio of these two wave numbers (or scales),

$$R_\beta = \frac{k_\beta}{k_R} = \beta^{1/10} U^{1/2} \epsilon^{-1/5}, \quad (14)$$

is known as the *Zonostrophy parameter* [25]. If we estimate  $\epsilon$  in dynamic equilibrium by equating it to the rate of energy loss due to dissipation, so that  $\epsilon \sim U^2/\tau_E$ , where  $\tau_E = H/\sqrt{\nu\Omega} \simeq E^{-1}\Omega^{-1}$  is the Ekman spin-down timescale (e.g., [29, 30]), we can approximate  $R_\beta$  by

$$R_\beta \simeq (\beta U \tau_E^2)^{1/10} = (2Ro^2 \beta_2 E^{-1})^{1/10}, \quad (15)$$

from which it is evident that large values for  $R_\beta$  are favored by strong  $\beta$ -effects, strong flows and weak Ekman dissipation (with large  $\tau_E$ ). Flows with small  $R_\beta$  are therefore known as *friction-dominated* to distinguish it from its *zonostrophic* counterpart, and are characterized by relatively weak flows, weak  $\beta$ -effects and/or strong Ekman dissipation. Since the zonostrophic regime is the one typified by strong, rectified zonal jet flows compared with the non-zonal flow components, we anticipate that strong eddy-driven jets will be most likely to occur in flows with strong  $\beta$ -effects and weak Ekman friction (small Ekman number).

It was first argued by Sukoriansky et al. (2007) [26], based upon the analysis of 2D simulations, that the zonostrophic regime is observed when  $R_\beta^s \gtrsim 2.5$ , where

$$R_\beta^s = \left(\frac{C_Z}{C_K}\right)^{3/10} \left(\frac{2^5 \beta U^5}{\epsilon^2}\right)^{1/10} = \left(\frac{C_Z}{C_K}\right)^{3/10} 2^{1/2} R_\beta. \quad (16)$$

Here,  $C_Z$  and  $C_K$  are supposedly universal constants determined from spectral analysis, with  $(C_Z/C_K)^{3/10} \approx 0.5$  [26, 31] such that  $R_\beta^s \approx 0.7R_\beta$ . In contrast, the regime is friction-dominated when  $R_\beta^s \lesssim 1.5$ . These approximate regime boundaries are represented in Figure 1. The intermediate case around  $R_\beta^s \sim 1.5 - 2.5$  is known as transitional flow, and is often found to share many qualitative properties (though not all) with fully zonostrophic flows.

#### 2.4. Dynamical similarity in experiments

Table 2 shows a comparison of the approximate sizes of various dimensionless groups which provide an indication of the likelihood of dynamical similarity between phenomena in the large-scale atmosphere, the oceans and typical laboratory conditions. This shows clearly that the Rossby and Burger numbers appropriate to the atmosphere and oceans (at least on the eddy-scale) are readily accessible under laboratory conditions, and this form of similarity is an important basis upon which laboratory analogues of large-scale atmospheric and oceanic phenomena are designed. The atmospheric and oceanic  $\beta$ -parameters, too, would seem to be accessible in the laboratory, at least using boundary topography to simulate some of the effects of planetary vorticity gradients.

The degree of similarity is not perfect, however, as revealed in significant differences between the aspect ratio  $D/L$  and parameters related to viscous and thermal diffusion ( $E$ ,  $Re$ , etc.). Planetary flows, particularly on gas giants, are characterized by a very large Reynolds number, a vanishing Ekman number and a small Rossby number, i.e., flows are both turbulent and rotationally constrained. Reaching  $E \ll 1$  or  $Re \gg 1$  in experiments is notoriously difficult. Doing so simultaneously is an even greater challenge, as increasing  $Re$  requires to increase the rotation rate to keep  $Ro$  small. Based on molecular viscosity and diffusivity, planetary parameters hence differ from those accessible in the laboratory by several orders of magnitude (see also Figure 1). However, it is important to note that, if approximate measures of *eddy*-diffusivity are used for the atmosphere and oceans, based on small-scale mixing processes (e.g. see [32, Chapter 9]), the values of  $E$  and (to a lesser extent)  $Re$  become more closely similar to those in the laboratory



**Table 2.** Comparison of the scale of various dimensionless parameters for the large-scale atmosphere of the Earth, eddy-scale and gyre-scale phenomena in the Earth’s oceans, and in a typical laboratory. The topographic  $\beta$ -effect,  $\beta_T$ , is calculated for a spherical shell at midlatitudes ( $45^\circ$ ). Details on planetary estimates of  $R_\beta^s$  are provided in the Supplementary Information. Starred items denote those estimated assuming a notional eddy diffusivity of  $10^{-2} \text{ m}^2 \text{ s}^{-1}$  in place of molecular quantities.

|  | Atmosphere<br>(Earth) | Oceans<br>(eddy)      | Oceans<br>(gyre)      | Deep<br>Atmospheres      | Exo-oceans<br>(e.g. Europa) | Laboratory         |
|--|-----------------------|-----------------------|-----------------------|--------------------------|-----------------------------|--------------------|
| $L$ (m)                                    | $\sim 10^6$           | $\sim 10^5$           | $\sim 10^7$           | $\sim 10^7$              | $\sim 10^6$                 | 0.1 - 10           |
| $D$ (m)                                    | $\sim 10^4 - 10^5$    | $\sim 10^3$           | $\sim 10^3$           | $\sim 10^6 - 10^7$       | $\sim 10^5$                 | 0.1 - 1            |
| $\beta$ ( $\text{m}^{-1}\text{s}^{-1}$ )   | $1.6 \times 10^{-11}$ | $1.6 \times 10^{-11}$ | $1.6 \times 10^{-11}$ | –                        | –                           | –                  |
| $\beta_T$ ( $\text{m}^{-1}\text{s}^{-1}$ ) | –                     | –                     | –                     | $1 \times 10^{-11}$      | $4 \times 10^{-11}$         | $0 - 10^2$         |
| $\eta$                                     | $10^{-2}$             | $10^{-2}$             | $10^{-4}$             | O(0.1-1)                 | O(0.1-1)                    | O(1)               |
| Ro   | 0.1                   | 0.1                   | $10^{-4}$             | $10^{-3} - \text{O}(10)$ | $10^{-3} - \text{O}(10)$    | $10^{-4} - \infty$ |
| E  | $10^{-10}$            | $10^{-8}$             | $10^{-8}$             | $10^{-14} - 10^{-12}$    | $10^{-14} - 10^{-9}$        | $10^{-7} - \infty$ |
| E*   | $\sim 10^{-6*}$       | $\sim 10^{-4*}$       | $\sim 10^{-4*}$       | $10^{-9}$                | $10^{-5}$                   | –                  |
| Bu   | 0.1                   | $10^{-2}$             | $10^{-6}$             | $10^{-8} - 10^{-2}$      | O(1) - $10^6$               | $10^{-2} - \infty$ |
| $\beta_1$                                  | 0.2                   | $10^{-2}$             | O(1)                  | $10^{-2}$                | $10^{-2} - 10^{-1}$         | $0 - \text{O}(1)$  |
| $\beta_2$                                  | O(1)                  | O(1)                  | $10^2$                | $10^{-3}$                | 0.1 - 10                    | $0 - \text{O}(10)$ |
| Pr   | $\sim 1^*$            | $\sim 1^*$            | $\sim 1^*$            | $\sim 1^*$               | $\sim 1^*$                  | $0.025 - 10^2$     |
| Ra   | $\sim 10^{21}$        | $\sim 10^{20}$        | $\sim 10^{20}$        | $0 - 10^{30}$            | $10^{26}$                   | $0 - 10^{11}$      |
| Ra <sub>F</sub>                            | $\sim 10^{29}$        | $\sim 10^{24}$        | $\sim 10^{24}$        | $\sim 10^{40}$           | $\sim 10^{31}$              | $0 - 10^{13}$      |
| Re   | $\sim 10^{12}$        | $\sim 10^{11}$        | $\sim 10^{12}$        | $\sim 10^{13}$           | $\sim 10^{12}$              | $\leq 10^5$        |
| Re*  | $\sim 10^{9*}$        | $\sim 10^{7*}$        | $\sim 10^{8*}$        | $\sim 10^{10*}$          | $\sim 10^{6*}$              | –                  |
| $R_\beta^s$                                | $\sim 1.4$            | $\sim 1.2$            | $\sim 1.2$            | $\sim 4 - 5$             | $\gtrsim 2 - 4$             | $0 - 3$            |

based on *molecular* diffusivities. Table 2 illustrates examples of the corresponding values of E and Re if a diffusivity of  $10^{-2} \text{ m}^2 \text{ s}^{-1}$  is used in place of the molecular values (shown as starred values), which lie significantly closer to the laboratory values. However, the concept of an eddy diffusivity is a controversial one in general and the effective value may be strongly dependent upon the details of the dynamics it represents and is quite uncertain.

In addition to  $E \ll 1$ ,  $\text{Re} \gg 1$ , and  $\text{Ro} \leq 1$ , simulating zonal jets require a large zonestrophy index, particularly for applications to the strongly zonated flows of gas giants. As represented in Figure 1, mid-latitude jets on gas giants are expected to be in the regime of zonestrophic turbulence with  $R_\beta^s \sim 4 - 5$ . In contrast, Earth’s oceans and atmosphere exhibit more moderate regimes with  $R_\beta^s \sim 1.2 - 1.4$ , corresponding to weak and meandering jets. For exo-oceans, estimating  $R_\beta$  is challenging given that no direct measurements of their flow is available and flow speeds are not constrained. Using flow speeds estimates from Jansen et al. [37] on one hand (based on a drag coefficient) and Cabanes et al. [14] on the other hand (based on Ekman friction) leads to zonestrophic index ranging from transitional to largely zonestrophic (see Supplementary Information). This leaves open the question of the relevant regime for icy moon oceans, although the friction-dominated regime seems irrelevant.

Reaching a large zonestrophic index experimentally is a further challenge: as noted in [33], because of the power 1/10 in the definition of the zonestrophy index (15), if all the other parameters are unchanged, increasing the typical velocity (and hence the Reynolds number) by

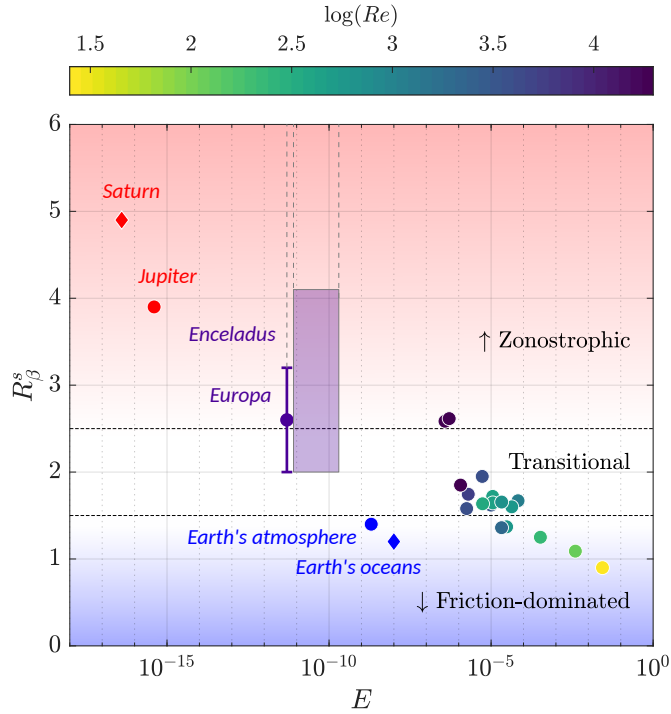


**Figure 1.** Zonal jets laboratory experiments in the non-dimensional parameter space Zonostrophy index  $R_\beta^s$  versus Ekman number  $E$ . The color of the symbols shows the Reynolds number. For the sake of comparison, we used similar definitions for all the experimental studies and planetary estimates (equation (16)). For all experimental studies,  $\epsilon$  is estimated by  $\epsilon \sim U^2 \sqrt{\nu \Omega} / (2H)$ . Details on planetary estimates are provided in the Supplementary Information. The vertical dashed lines for icy moon oceans indicate that the represented zonostrophy index is a lower bound due to the lack of constraints on their flow speed (see Supplementary Information). Figure adapted from [33, Figure 1], with the addition of experimental data from [34–36].

ten only increases the zonostrophy index by a factor  $10^{1/10} \sim 1.26$ ! Most experiments to date lie in the transitional or friction-dominated regimes, as represented on Figure 1. More strongly-zonated regimes were recently reached by [33, 38, 39], as discussed in Section 6.3.

For thermally-driven flows, a further important dimensionless parameter is the Prandtl number. This is often large in the laboratory, because of the fluids in common use (based typically around water ( $\text{Pr} \simeq 7$ ) [40] or silicone oils ( $\text{Pr} \sim 10$ -100 or greater) [41], cf. [42, 43]). For geophysical flows, however, the appropriate value for  $\text{Pr}$  is less clear. This is because it is common to parametrize small-scale mixing in the atmosphere or oceans as a form of diffusive process via “eddy viscosities” and other coefficients. However, the relative efficiency of such processes for heat and momentum is often dependent on the problem, with effective Prandtl numbers ranging from significantly less than unity to much larger values (e.g. see [44]).

### 3. Basic theories and properties of jet flows

Jet-like flows can be driven via the rectified effect of generalised Reynolds stresses associated with eddies. This is an inherently nonlinear process that entails eddies adopting a particular

flow structure that results in systematic correlations between different velocity and buoyancy components in such a way as to result in transfer of linear (or angular) momentum.

### 3.1. How are rectified zonal flows generated?

For simplicity we use the Boussinesq equations on the beta-plane ([4, Chapter 2]). We hence work in a plane tangent to a reference latitude, with local Cartesian coordinates  $(x, y, z)$  representing the East-West, North-South, and local vertical coordinates, respectively. We denote  $\mathbf{u} = (u, v, w)$  the corresponding velocity. Let us decompose the fields into a zonal ( $x$ -) mean (to be denoted with an overbar) plus a perturbation (denoted with a prime). Following e.g. [45] and [4], the equation governing the zonal mean velocity  $\bar{u}$  can be written in the Transformed Eulerian form

$$\frac{\partial \bar{u}}{\partial t} - \overline{v^*} \left( f - \frac{\partial \bar{u}}{\partial y} \right) + \overline{w^*} \frac{\partial \bar{u}}{\partial z} = -\nabla \cdot \mathbf{F} + \overline{\mathcal{F}_u}, \quad (17)$$

where  $f = 2\Omega$  is the Coriolis parameter,  $\overline{\mathcal{F}_u}$  represents direct body forces and dissipation, primed quantities denote departures from a zonal ( $x$ -) mean and  $\mathbf{F} = (0, F^{(y)}, F^{(z)})$  is the Eliassen–Palm flux (effectively anti-parallel to the generalised Reynolds stress and flux of zonal momentum), defined as

$$F^{(y)} = \left( \frac{\partial \bar{u}}{\partial z} \frac{\overline{v' b'}}{\left( \frac{\partial \bar{b}}{\partial z} \right)} - \overline{u' v'} \right), \quad (18)$$

$$F^{(z)} = \left( \left[ f - \frac{\partial \bar{u}}{\partial y} \right] \frac{\overline{v' b'}}{\left( \frac{\partial \bar{b}}{\partial z} \right)} - \overline{w' u'} \right). \quad (19)$$

Here  $b$  is the buoyancy, defined as  $b = -g\delta\rho/\rho_0$  where  $\rho$  is density with reference value  $\rho_0$ ,  $\delta\rho = \rho - \rho_0$  and  $g$  the acceleration due to gravity.  $\mathbf{u}^* = (0, \overline{v^*}, \overline{w^*})$  represents the Transformed Eulerian Mean (TEM) meridional circulation, which approximates to a Lagrangian mean circulation that more cleanly separates the effects of eddies from a more conventional zonal mean circulation, and is defined by

$$\overline{v^*} = \bar{v} - \frac{\partial}{\partial z} \left( \frac{\overline{v' b'}}{\left( \frac{\partial \bar{b}}{\partial z} \right)} \right), \quad (20)$$

$$\overline{w^*} = \bar{w} + \frac{\partial}{\partial y} \left( \frac{\overline{v' b'}}{\left( \frac{\partial \bar{b}}{\partial z} \right)} \right). \quad (21)$$

The TEM circulation  $\overline{\mathbf{u}^*}$  takes account of the partial cancellation of the Eulerian zonal mean circulation and the meridional overturning circulation induced by the eddies, and is typically dominated by a balance of zonal mean advection and diabatic heating or cooling. The Eliassen–Palm flux plays the role of a generalised Reynolds stress, whose divergence represents the effective stress acting on the zonal mean velocity due to the action of eddies. The resulting generalised Reynolds stress covariance may be divergent where waves or eddies are transiently growing or decaying in amplitude with time, and/or are being actively generated or dissipated. Such divergences lead to the net deposition of momentum, which can ultimately manifest itself as a rectified zonal flow or jet (e.g. [4, 45, 46]).

### 3.2. *Jet strength and direction?*

The direction and strength of the rectified zonal flow may depend upon the wave-like properties of the eddies (e.g. see [4]). The sign of  $\nabla \cdot \mathbf{F}$  in steady, forced or dissipated eddy flows, for example, depends on whether the waves or eddies are actually being locally forced or dissipated. For waves with a well defined phase velocity,  $\mathbf{c}$ , the theory suggests that dissipating waves will tend to deposit rectified (pseudo-)momentum in the same sense as  $\mathbf{c}$  in the zonal mean, especially in the vicinity of critical layers where the flow velocity  $\bar{\mathbf{u}}$  approaches  $\mathbf{c}$ . At latitudes or radii where waves are being energised by local forcing, however, zonally-averaged wave (pseudo-)momentum is being radiated away meridionally from the forcing region in the direction of the group velocity, leading to the generation of an eddy-induced zonal flow which is of opposite sign to  $\mathbf{c}$ ; e.g. see [4, 45, 46] for further details.

For weakly nonlinear flows, the rectified zonal flow effectively results from the quadratic nonlinear self-interaction of the eddies or waves. So this would suggest that the magnitude of  $|\bar{u}|$  should scale roughly as  $O(\alpha^2)$ . For dissipating waves, however, the dissipation may be enhanced as a critical line (where  $\bar{u} \sim c$ ) is approached and the wavelength normal to the critical line decreases. This would indicate that  $|\bar{u}| \lesssim |\mathbf{c}|$  for dissipating waves (e.g. see [4, 45, 46] and references therein).

### 3.3. *Jet structure and width?*

It is also of interest to understand what determines the vertical and lateral structure of eddy-induced zonal jets and the length scales associated with the variations of  $\bar{u}$  in height and the direction transverse to the jet. The spatial structure of the forcing likely plays an important role, while for stratified flows the form of the dissipation and the vertical location of any critical layers affect the vertical structure of  $\bar{u}$ . For rapidly rotating flows, eddy forcing would be expected to favour the generation of barotropic structure of  $\bar{u}$  in the vertical. In the horizontal, however, Rossby wave steepness (effectively measured by  $\beta_2$ , cf Eq. (9)) is likely to be important, suggesting the possible significance of the Rhines scale  $L_R \sim 1/k_R$  (see Eq. (12)) within the flow. This may depend on various factors but is likely to be significant in flows where multiple, persistent, parallel zonal jets emerge.

Such effects are observed in atmospheres and oceans, for example, where eddies generate substantial jet-like currents such as certain features of the tropospheric jet stream on Earth and the equatorial undercurrent in the oceans, as well as the multiple zonal jet streams on Jupiter and Saturn, and has also been suggested as contributing to the strong equatorial super-rotating flows on Venus and Jupiter. The process has been studied on a laboratory scale for many years, initially in relation to discussions on the effects of “negative viscosity” as a representation of the effects of nonlinear interactions between turbulent eddies and zonal flows (e.g. [47]).

### 3.4. *Potential Vorticity Mixing*

Potential vorticity (PV) is likely to be a conserved quantity in low  $Ro$ , low  $E$  planetary and stellar fluid settings [4]. Strong turbulent mixing in a latitudinal band may then act to homogenize  $2\Omega/h$ , the planetary potential vorticity, yielding some mixed value  $\bar{q}$  everywhere in the band. The relative axial vorticity is then predicted to vary as

$$\zeta = \bar{q} h(s) - 2\Omega. \quad (22)$$

If it is further assumed that  $\zeta$  is comprised of azimuthal axisymmetric zonal jet flows, then (22) provides upper bounding estimates on the strength of zonal jet flows in which all the planetary

PV reservoir in the mixed latitudinal band is converted into zonal jet motion [48]. See for example the experimental study of [49] for discussion of laboratory zonal flows potentially generated by potential vorticity mixing in low Rossby number turbulence.

#### 4. Experimental Techniques: Metrology

Zonal jet experiments have been carried out for the past 50 years (e.g., [15, 50, 51]). In the majority of these, the turbulence is mechanically-driven (e.g., [15, 36, 38, 49, 52]), with a smaller subset driven by buoyancy (e.g., [53–55]) or Lorentz forces (e.g., [56]). Fewer still are driven by waves and wave turbulence (e.g., [51, 57, 58]). Irregardless of the forcing, zonal flows can be found to emerge in these differing laboratory systems, as detailed in Sections 5 and 6. However, relatively few to date have generated jets in the zonostrophic regime due to the difficulty in generating large  $R_\beta$  values, per Eq. (15).

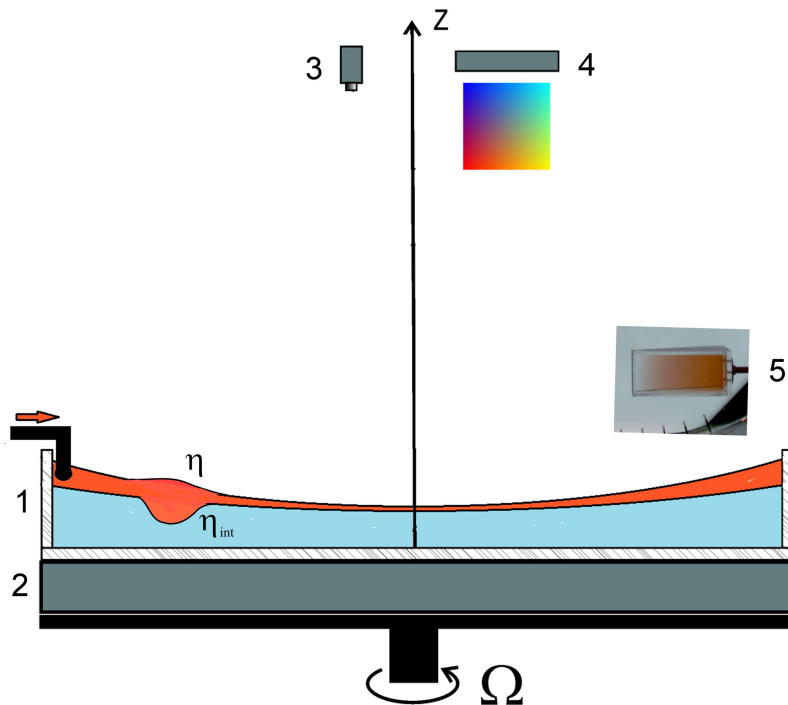


**Figure 2.** Schematic diagram of the experimental arrangement using Altimetric Imaging Velocimetry and Optical Thickness Velocimetry in rotating baroclinic two-layer flows: (1) rotating tank, (2) light panel for the optical thickness measurements, (3) video camera, (4) light source with color mask, and (5) wedge-shaped cuvette used for the calibration of the optical thickness.

Developments of new measuring techniques and digital video and data processing equipment have allowed laboratory experiments to progress from mostly qualitative and observational to quantitative; with resolutions comparable to those of numerical simulations (at least in 2D). It is often desirable to resolve all significant scales, from the viscous scale of an order of 1 mm up to the scale of the experimental tank (typically 1-2 m).

Particle image velocimetry (PIV) is a very popular technique for non-intrusive, quantitative and qualitative flow visualization, and has been widely used in experiments with fluids [59] including GFD rotating fluids for decades. Small reflective particles of neutral density are seeded in the water. For two-dimensional PIV (mostly used in rotating flows) the particles are visualized in a plane illuminated by a laser. Owing to the Taylor–Proudman theorem, motions in rapidly-rotating fluids are indeed expected to be almost invariant along the rotation axis, visualising them on a plane orthogonal to the rotation axis should hence be representative. A camera – usually attached to the rotating frame – records particle motion on the laser sheet, and particle displacement is calculated by subdividing the images into sub-regions called interrogation areas, so that it is actually the displacement of groups of particles that is calculated. This is done using cross-correlation of two consecutive images. The displacement per time gives a space-resolved, Eulerian velocity field, from which gradient-based quantities (e.g., vertical vorticity) can be calculated (see Figure 12 (b)). Both commercial and open-source PIV software are now widely available to perform post-processing of images (see [60] and references therein).

By design, the size of interrogation areas ultimately determines the spatial resolution, or rather the range of scales that PIV can resolve. In terms of temporal resolution, the typical flow velocities determine the maximum time step  $\Delta t_1$  between images of a given pair for the cross-correlation to be successful. But the time between two pairs,  $\Delta t_2$  can be chosen independently. For instance,  $\Delta t_2$  can be chosen small (equal to  $\Delta t_1$ ) if the goal is obtain time-resolved velocity fields of a turbulent flow. If on the other hand the goal is to follow the very slow evolution of the zonal flow, then one can choose  $\Delta t_2 \gg \Delta t_1$ . Of course, what limits the possibility of recording images with small time steps over very long times is the available memory of the system and its data streaming capabilities. Note that typical flow velocities in zonal jets experiments ( $\text{mm s}^{-1}$  to few  $\text{cm s}^{-1}$ ) require only moderate temporal resolution (moderate  $\Delta t_1$ ), hence CCD and CMOS based digital cameras are commonly employed for PIV measurements.

In meter-scale GFD experiments, particles consisting of hollow coated glass spheres of approximately 10-100  $\mu\text{m}$  work very well. To obtain images of the highest possible quality, it is also possible to use fluorescent particles in combination with a band-pass filter on the camera to image only the light emitted by the particles (see [39, Supplementary Movie 1]). To improve measurements, the most common technique is to pre-process images before the actual cross-correlation (e.g., removing the background by subtracting a time-averaged image), however, the images have to be of the highest possible quality beforehand. Note also that if the laser sheet is visualised through a paraboloidal free-surface, images need to be corrected from the optical distortion induced by the paraboloidal free-surface [61].

An alternative technique developed specifically for rotating fluids with free surface is the Altimetric Imaging Velocimetry (AIV). It takes advantage of a parabolic shape of the surface when in equilibrium and measures the perturbations of this shape due to the flows. The AIV has evolved from the gray-scale optical altimetry [62] by incorporating color coding of the surface slope components [63, 64]. The hardware for AIV includes a video camera and a light source with color mask located above the surface of water on the rotating table. The camera records reflection of multi-color light by the surface of water. Two components of the gradient  $\nabla\eta = (\partial\eta/\partial x, \partial\eta/\partial y)$  of the surface elevation  $\eta$  are measured in the horizontal plane  $(x, y)$ . This is unlike satellite altimetry which measures the surface elevation rather than its slope. However, the velocity computation is similar in both cases. Velocity of the flow is computed using the quasi-geostrophic (QG) approximation:

$$\mathbf{u} = \frac{g}{f_0} \hat{\mathbf{z}} \times \nabla\eta - \frac{g}{f_0^2} \nabla\eta_t - \frac{g^2}{f_0^3} J(\eta, \nabla\eta), \quad (23)$$

where  $\hat{\mathbf{z}}$  is the vertical unit vector,  $f_0 = 2\Omega$  is the Coriolis parameter,  $\Omega$  is the rotation rate of the tank and  $J(A, B)$  is the Jacobian operator. The first term in the rhs of (23) is the geostrophic velocity, the second and third are higher order terms due to time tendency and advection. Thus, the AIV technique visualizes the surface, measures its slope and allows one to compute the barotropic QG velocity in virtually every pixel of the image.

A baroclinic two-layer fluid is often used in the experiments. In this case, AIV can be used in combination with the optical thickness velocimetry (OTV). The OTV is based on the absorption of light by dye dissolved in water. The upper (or lower) layer is dyed by a red (or green) food dye and illuminated by uniform white light provided by a light panel under the tank. The variations of thickness of the dyed layer due to the flow are visible to the camera above; color saturation in each pixel of the image can then be related to the thickness of the layer,  $h_1$ . Baroclinic geostrophic velocity is computed using thermal wind equation:

$$\mathbf{u}_{bc} = -\frac{g'}{f_0} \hat{\mathbf{z}} \times \nabla h_1, \quad (24)$$

where  $g' = g(\rho_2 - \rho_1)/\rho_2$  is the reduced gravity,  $\rho_1$  and  $\rho_2$  are the densities of the upper and lower layer, respectively. Baroclinic velocity in the QG approximation can be obtained from (23) replacing  $\eta$  by  $-h_1$ . OTV and AIV can be used almost concurrently when the upper and lower lights are alternated [65]. Thus, the baroclinic two-layer system is fully resolved with the upper layer velocity  $\mathbf{u}_1 = \mathbf{u}$  and lower layer velocity  $\mathbf{u}_2 = \mathbf{u} + \mathbf{u}_{bc}$ .

In the experiments (e.g., [40]) where density gradients are created by heating or cooling, thermal radiometry proved to be useful. Infra-red camera can provide snapshots of the temperature field at the surface; the temperature is converted into density using the equation of state for water. Density gradient, in say, the radial direction can then be related to the vertical shear of the zonal velocity using the thermal wind equation (see also [66]).

In the next section we review a range of experiments that have demonstrated and explored the applicability of many of the theoretical concepts and issues introduced in the previous Section 3. Experiments may be distinguished in their approach towards generating and maintaining eddies, with or without the presence of background rotation or stratification, and have explored in both qualitative and quantitative terms some of the mechanisms that lead to the generation of zonal jet flows. Different configurations of experiments have investigated both the structure of eddy-driven jet flows subject to very different forcing processes and the dependence of their strength, direction and width on various scaling parameters.

## 5. Zonal Jets Experiments: localized forcing

### 5.1. “Moving flame” experiments

Some of the earliest experiments to demonstrate nonlinear rectification effects in a fluid excited by waves were those intended to demonstrate the “moving flame” effect [67]. In these experiments, a localized heat source (such as a bunsen burner) was rotated underneath a cylindrical vessel containing a fluid that was initially stationary. The heat source would excite a thermal (buoyancy) wave that would translate in the direction of the moving heat source. For various reasons (such as due to the inertia associated with thermal diffusion), the thermal wave could develop a phase shift with height, so that the associated vertical and zonal velocity field would acquire a tilt, and hence a significant  $\overline{u'w'}$  Reynolds stress. As the thermal wave propagates with height above the heat source, it dissipates and leads to a rectified acceleration of the zonal mean state of the fluid which develops a significant streaming flow in the opposite direction to the motion of the heat source.

Several versions of this kind of experiment were investigated during the 1960s and 1970s as possible analogues of the thermal tide on Venus, which was then thought to be the main driver of the strong super-rotation of its atmosphere [68–70]. The results did, indeed, demonstrate various forms of zonal streaming in fluids of widely varying Prandtl number, associated with the zonal tilt and phase shift of thermally driven gravity waves and convective cells excited by different forms of heat source (including both boundary and internal heat sources), though a convincing quantitative theory to account for the observed flows was slow to emerge. The simplest theories relied on diffusive inertia to produce the required tilt of the thermally excited waves with height and resulting Reynolds stresses, which were then expected to lead to zonal flows comparable in magnitude to the phase speed of the heat source. In a few cases, however, much stronger flows were observed [69], as would be necessary to account for the observed super-rotation of Venus’s atmosphere, which is at least 30 times faster than the motion of its semi-diurnal thermal tide [71, 72]. In practice, however, this turned out to be at least partly driven by temperature variations in surface tension at the free surface of the fluid, so was of less interest as an analogue of planetary flows. Even those flows for which surface tension effects were not significant relied on molecular heat diffusion to provide the thermal inertia needed to create vertical phase shifts, which limits the degree to which they can emulate planetary-scale phenomena. But nevertheless these experiments played an important historical role, serving to excite interest in exploring more general mechanisms for driving zonal streaming effects due to eddies.

## 5.2. *Barotropic jet flows with Rossby wave forcing*

Another important class of experiments excited eddy-driven jets in homogeneous, barotropic flows by directly forcing eddying motions but mostly without explicit zonally-symmetric forcing. In a prescient series of experiments, [51] was able to demonstrate the formation of barotropic, eddy-driven zonal flows in a cylindrical water tank with a flat bottom and centrifugally-deformed, parabolic free surface to induce a topographic  $\beta$ -effect. By using relatively simple localized stirring, either via oscillating mechanical plates or streams of air bubbles, a train of Rossby waves were generated that spontaneously formed a rectified zonal streaming flow. [51] noted that the induced zonal flow was prograde at the radius where the forcing was introduced and weakly retrograde on either side of the forcing.

In subsequent studies [15, 73], a rotating, cylindrical tank of water or a silicone oil was used with a centrifugally deformed free surface (to create a polar  $\beta$ -plane) and an ingenious method of exciting topographic Rossby waves of a fixed wavenumber ( $m = 6$ ), frequency and phase speed  $c$  via a source-sink technique developed by A. McEwan (see Figure 3). This was used to demonstrate the development of an eddy-driven jet, aligned along the (azimuthal) geostrophic contours. The experiments were able to show how the  $m = 6$  forcing would excite a zonally propagating Rossby wave that would radiate away from the region of source-sink forcing, producing a zonal flow at the forcing radius that was in the opposite sense to  $c$  for the forced travelling wave. This rectified flow was flanked on either side by weaker zonal jets that were in the same sense as the motion of the forced wave (see Figure 4). The mean zonal flow  $\bar{u}(r)$  was anticorrelated with the divergence of the Reynolds stress  $\overline{u'v'}$ , as expected from the discussion above.

They also investigated the scaling of the induced zonal velocity with the strength of the forced eddies and showed that the forcing pattern needed to propagate zonally at the same rate as the corresponding Rossby wave pattern in order to produce a strong response. The resulting rectified zonal flow scaled roughly quadratically in amplitude with the amplitude of the wave forcing and was interpreted in terms of a modulational instability of Rossby wave packets. In addition, the behavior of potential vorticity mixing was also investigated and shown to be consistent with the eddy driving mechanism.



However, these experiments did not investigate the formation of multiple zonal jet patterns and the associated length scales and their dependence on experimental parameters.

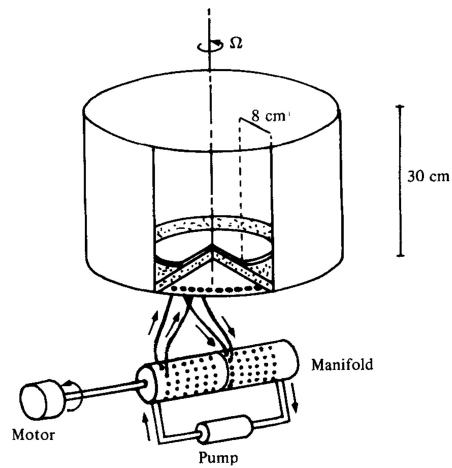
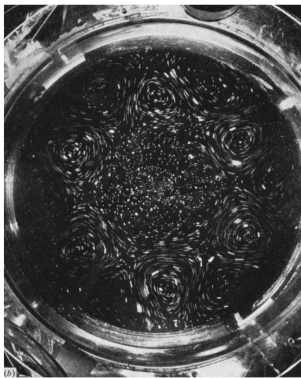
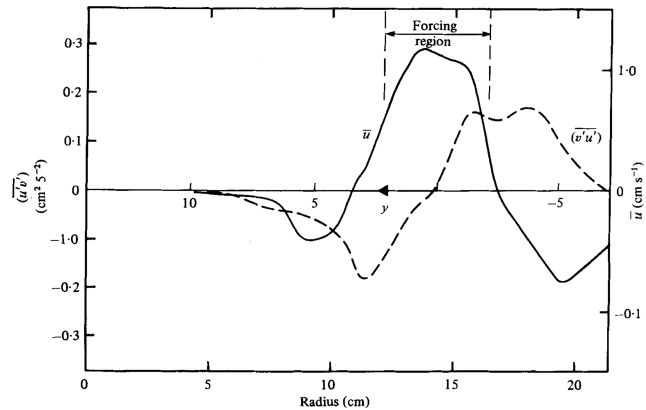


**Figure 3.** Schematic diagram of the experimental arrangement to create trains of travelling wave-like eddies to force zonal flows using mass sources and sinks in the bottom of the tank at a fixed radius towards the outer boundary of a cylindrical tank (taken from [15] and [73] with permission).



(a)



(b)

**Figure 4.** (a) Surface streak photograph of a typical equilibrated flow in the experiments of [73] forced by a wavenumber  $m = 6$  travelling wave pattern. (b) Profiles of  $\bar{u}$  and  $\overline{u'v'^r}$  for a similar equilibrated flow. Experiment (a) corresponds to  $f = 9.74 \text{ s}^{-1}$ ,  $\gamma = ck^2/\beta = -0.36$ ; (b) corresponds to  $f = 8.46 \text{ s}^{-1}$ ,  $\gamma = -0.36$ . Reproduced from [73] with permission.

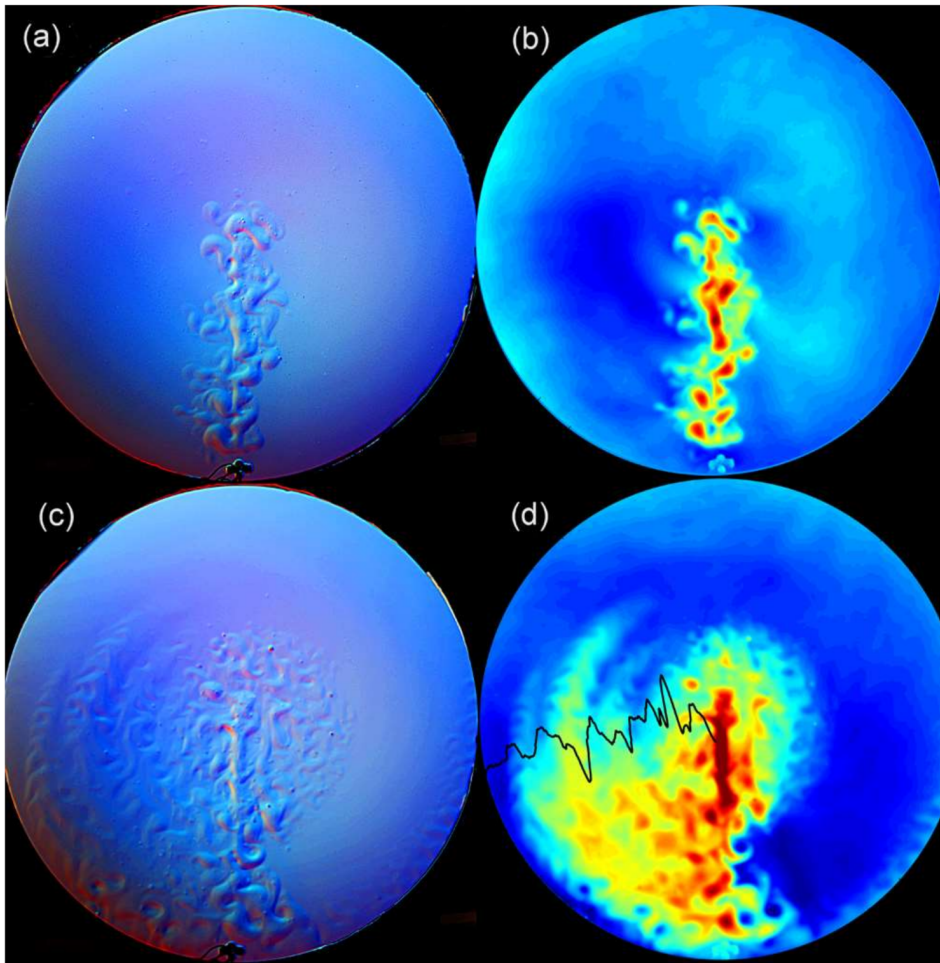


**Figure 5.** Flow on the polar  $\beta$ -plane generated by a linear heater: altimetric color images (a, c) and surface elevation derived from altimetry (b, d). Insert in (d) shows a radial profile of the azimuthal velocity (black line).

### 5.3. Zonal flows excited by Rossby wave radiation from localized buoyancy sources and boundary currents

To get an insight into dynamics of jets and especially the interplay between jets, eddies and Rossby waves, it is often desirable to observe the evolution of flows created by localized forcing from rest. Typically, we don't have this opportunity in the ocean or in the experiments where jets are created by multiple eddies/Reynolds stresses in the entire domain (Section 6).

An initial response of fluid to a spatially localized source is described by a linear theory of Rossby waves (e.g. [54, 74–76]). This response is called the  $\beta$ -plume and is a gyre-like circulation consisting of two zonal jets flowing in opposite directions which are reconnected in the area of the source as well as at the front of the plume. The  $\beta$ -plume extends westward of the source area where longer waves propagate while to the east of the source, shorter waves create a periodic wavy pattern. The two jets in the the  $\beta$ -plume are flowing along the slopes of the ridge on the surface; the ridge being an extension of the elevated surface above the source. While initial

dynamics is linear, the finite amplitude circulation is soon established. Thus Rossby waves provide a path for creation of the zonal flows. It is difficult to observe Rossby waves in the laboratory with any techniques other than altimetry. The illustrations of the barotropic and baroclinic  $\beta$ -plumes generated by sources or sinks on the polar  $\beta$ -plane are given in [54, 76, 77]. Oceanographic examples of localized forcing include local mixing, surface cooling/heating, outflows, eddies, and meanders of coastal currents.

A series of papers by [35, 54, 78] investigates baroclinically unstable flows where multiple  $\beta$ -plumes were observed. The experiments were designed to model coastal currents flowing along the eastern shores of oceans. These currents form meanders due to a baroclinic/frontal instabilities which, in turn, emit Rossby waves and shed eddies. The perturbations then propagate westward and create alternating zonal jets. The laboratory flows were created using two different methods. In the first method, a source placed at the wall of the tank continuously delivered fresh water on top of a thick layer of saline water. A radial barrier was used to model an eastern coast. Fresh water flows as a coastal current along the wall, turns to the north, toward the pole, along the barrier, then turns around the tip of the barrier and flows back to the South along the other side of the barrier and eventually continues flowing along the wall of the tank. In the second method, a heater placed along the radius of the tank near the bottom was used. The heater creates an upwelling of warm water which becomes unstable; the flow then evolves very similarly to that generated by a coastal current.

Figure 5 shows altimetric images of the flow in the beginning (top row) and at the end (bottom row) of the experiment. Warm water from the heater rises to the surface and creates elevated surface topography. Note the current above the heater flows according to geostrophy, northward and then southward following the outline of the heater just like the coastal current flows around a barrier. Eventually, multiple plumes, ridges on surface, each consisting of counter-flowing jets on their slopes, form westward of the heater. We can also see some interesting details of the Rossby wave propagation. Warm anticyclonic eddies are characterized by an elevated surface (yellow-red color); the baroclinic flow comprised of the eddies can be easily identified. However, if we look closely at the fluid westward or eastward of the baroclinic area we can also see the larger –scale perturbations there. These perturbations are barotropic Rossby waves propagating in the homogeneous fluid. The difference between the wave patterns westward and eastward of the heater reveals the east-west asymmetry of the Rossby waves. The perturbations to the west of the front of the baroclinic area are in the form of annular modes with small zonal wavenumber; in contrast, the perturbations to the east of the baroclinic area are of relatively high zonal wavenumber. This can be easily understood from the textbook theory of Rossby waves which demonstrates that only short wavelength waves are capable of propagating to the east. These observations illustrate the mechanism of  $\beta$ -plume formation where fast long Rossby waves emitted by (quasi) stationary perturbations propagate to the west and establish an almost zonal plume circulation. This circulation provides an initial deformation field which, in turn, affects the distribution of the baroclinic eddies which results in their chain-like arrangements. Note that there is no transport of eddies to the east (except perhaps along the wall of the tank where a coastal currents develops later in the experiment).

Finally, paper [35] investigates  $\beta$ -plume generated jets in the system where  $\beta$  changes sign thus creating critical latitudes. The experiments were designed to model Jovian jets in the weather layer lying on top of dynamic topography created by deeper flows in the convecting interior. In the experiments,  $\beta$  due to the parabolic surface was modified by a bottom topography which had a tent-shaped radial cross section. This created a negative  $\beta$  zone in the midlatitudes of the tank. The flows were forced by a submerged source pipe injecting fluid along one radius. In the negative  $\beta$  zone, long Rossby waves propagate eastward, “upwind” against westward current. This flow is characterised by a hydraulic-like control such that the analogue of the Mach number for Rossby

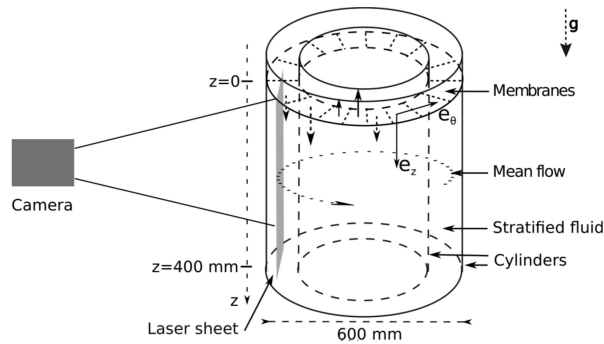


**Figure 6.** Schematic layout of the internal gravity wave experiment of [80]. ©American Physical Society. Used with permission.

waves,  $M_R = u/(-c_x) = 1$ , where  $u$  is the zonal velocity and  $c_x$  is the intrinsic zonal phase speed of the waves (before Doppler shifting). This parameter occurs in a range of theories including those of jet spacing [27], hydraulic control [24], and shear instability [79]. A similar result was obtained in the experiments by [39] where  $M_R$  goes to unity for their forced Rossby waves.

## 6. Zonal Jets Experiments: global forcing

Section 5 focuses on experiments where the forcing, regardless of its nature, is localised in space. In the present section, we turn to experiments where the forcing is global, and waves and eddies are excited in the entire domain. This configuration is arguably more relevant to some planetary applications (e.g., fully convective interiors).

### 6.1. Wave forcing in stably stratified flows

One of the conceptually simplest contexts in which zonal mean flow acceleration may arise via the interaction of waves or eddies relates to the generation, propagation and dissipation of internal gravity waves in a stratified fluid. The observations of strong zonal flows in the Earth's stratosphere that oscillate on a roughly 2 year period (e.g. [81]) led to some early pioneering theoretical work on mechanisms to drive zonal flows through the forcing and dissipation of vertically propagating internal waves (e.g. [82–85]). In particular, the effect of competing eastward and westward propagating waves, driven upwards from the tropical troposphere, was suggested to lead to an alternating dominance of wave streaming effects successively driving eastward and westward zonal flows as the zonal flow structure would successively promote and inhibit the upward propagation of westward and eastward propagating waves in turn.

Our understanding of such complex oscillatory flows and the development of theoretical models of the QBO is based on assumptions of how individual, weakly nonlinear, vertically propagating internal waves interact and energise a zonally symmetric zonal flow. It is somewhat surprising, therefore, that until recently, experimental investigations of this kind of phenomenon have tended to explore rather complicated configurations of wave forcing that are spatially inhomogeneous and/or complex in time [57, 86, 87]. The reasons for this are partly historical in that experiments were typically motivated by a desire to reproduce an analogue of a complex geophysical phenomenon, such as the QBO itself (see also [88, 89]). But one of the particular strengths of an experimental approach is the possibility of isolating particular fundamental processes in a real fluid and exploring their sensitivity to and dependence upon different experimental conditions.

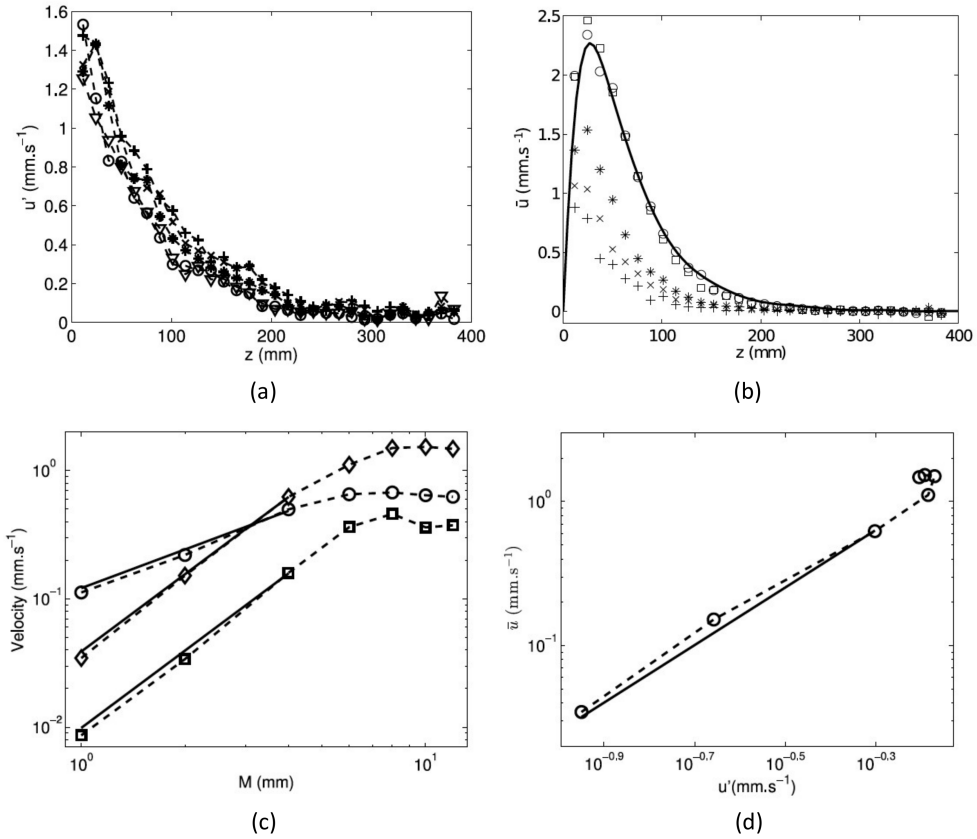


**Figure 7.** Vertical profiles of (a) horizontal wave amplitude  $u'$  and (b) mean flow  $\bar{u}$  at various times, showing convergence towards a fit to a theoretical model based on [83] (solid line in (b)); (c) dependence of the amplitude of the mean flow  $\bar{u}$  (diamonds), dominant wave mode  $u'(k_x)$  (circles) and its first harmonic  $u'(2k_x)$  (squares) of the internal wave at a depth of  $z = 64$  mm below the top surface as a function of the forcing amplitude  $M$ ; (d) dependence of the amplitude of the mean flow  $\bar{u}$  on the amplitude  $u'$  of the internal wave at a depth of  $z = 64$  mm below the top surface. Solid line indicates a quadratic fit to  $\bar{u}(u')$ . ©American Physical Society. Used with permission.

In a recent study [80], almost the simplest possible configuration of a vertically propagating, quasi-two-dimensional internal gravity wave was investigated to explore the validity of some of the assumptions underlying wave-zonal flow interactions in simple (and not so simple) models. The experiment was inspired by the ingenious and influential set of experiments by [57] in a form similar to that used by [86], in which an annular channel was filled with water that was stably stratified with a salt concentration that varied linearly with height. A single, monochromatic travelling wave of a given zonal wavenumber  $k_x$ , frequency  $\omega$  and displacement amplitude  $M$  was imposed at the top boundary by the use of a series of segmented chambers covered with a rubber membrane, each of which could be elevated or depressed by a set of actuators. A schematic of the apparatus is shown in Figure 6. The flexible top boundary was able to launch a monochromatic, downward-propagating internal gravity wave that would then decay with depth as it was dissipated by the fluid viscosity.

The impact of this downward propagating and dissipating wave in generating a zonal flow was then explored as a function of depth and parameters such as the forcing amplitude  $M$  at the top boundary and the local internal wave amplitude  $u'$ . Some examples are illustrated in Figure 7, which show (a) how the wave amplitude varies with depth, (b) the corresponding vertical profile of mean zonal flow, (c) how the strength of the mean zonal flow, the fundamental and the second harmonic of the forced wave varies with  $M$  at a fixed depth and (d) how the strength of the rectified zonal flow  $\bar{u}$  varies with local internal wave amplitude  $u'$ . Viscous damping evidently causes the wave to decay with depth below the forcing over a typical length scale of 10-20 cm. This leads to an eddy-driven zonal flow which peaks in strength just below the forcing and decays with depth further down. Figure 7(c) shows how the amplitude of the directly forced wave  $u'(k)$  scales linearly with forcing amplitude  $M$  until it saturates at large  $M$ , while  $\bar{u}$  and the second wave harmonic  $u'(2k)$  scale quadratically with  $M$ , as expected for nonlinear interactions. This quadratic dependence of  $\bar{u}$  on wave amplitude  $u'$  is seen also to hold locally, as evident in Figure 7(d).

## 6.2. Orbitally-forced flows

Banded azimuthal flows can also be excited by way of mechanically-imposed “orbital” forcings that generate inertial waves and container-scale modes [58, 90]. In planetary settings, these arise in association with an externally-imposed body force, such as the effect of gravitational forces on a planetary or stellar interior due to an orbiting moon or planet. The excited inertial waves and oscillations can resonate and reach large amplitude within a confined cavity if the forcing frequency matches that of an inertial eigenmode. The existence of such tidal resonances and the consequent interactions with viscous boundary layers (essentially modified Ekman and Stewartson layers at the surface of spheroidal cavities) can lead to the formation of internal shear layers and nonlinear interactions that can non-locally transfer kinetic energy into zonally-symmetric flows, even though the forcing may be strongly nonaxisymmetric. In theory, the strength of zonal flows driven by strongly nonlinear inertial waves can reach large amplitudes as viscous dissipation tends towards zero (e.g., [91]).

Orbital forcings investigated via laboratory experimentation include precession of the rotation axis, libration and tidal deformation. In precession and latitudinal libration experiments the container’s rotation vector is fixed in place. Instead, it precesses [92–94] or latitudinally nods in space [95]. In the case of longitudinal libration, the purely axial angular velocity oscillates sinusoidally in time around its mean value [96–99]. In tidally driven experiments, the fluid shell is sinusoidally deformed as it passes through a simulated tidally-distorted gravity field [100, 101].

Figure 8 shows shear layers in (a, b) librating [99], (b) tidally-deforming, and (c, d) precessing [92, 100] laboratory experiments. In all three cases, nonlinear inertial wave dynamics drive the development of strong zonal shear layers. In panel (a), the predicted inertial shear layers are demarcated in white dot-dashed lines, and the locations of the critical layers on the inner boundary are denoted by the dot-dashed maroon lines. Panel (b) shows the same image sans the guiding lines. These experimental libration images show that the predicted geostrophic zonal shear structures correspond well with the locations of the critical latitudes, and the inclined shear structures map out the predicted structure of oscillating inertial mode shear layers.

Figure 8(c) shows shear structures from the tidal deformation experiments of [100] in which  $m = 2$  inertial waves were excited by deforming a water-filled, rotating, spherical cavity between a pair of rollers that could be independently rotated at a controllable rate. The resulting flow patterns were visualized using kalliroscope particles and velocity fields in the equatorial

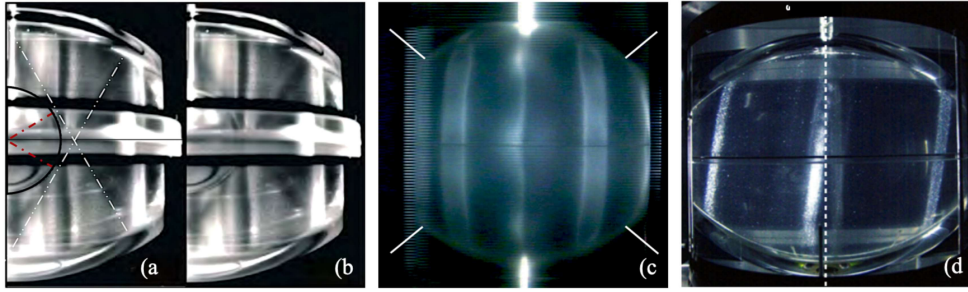


**Figure 8.** Kalliroscope images of zonal shear flows in orbitally-forced (a, b) libration [99], (b) tidal deformation [100] and (c) precession experiments [92]. (a, b) Reproduced from [99] with permission from Wiley ©2017 American Geophysical Union. (c) Reprinted with permission from [100] ©2010 American Physical Society. (d) Reproduced from [92] with permission from Wiley ©2001 American Geophysical Union.

plane measured using PIV. The shear pattern in Figure 8 (c) shows the formation of axisymmetric geostrophic flows, aligned along cylinders coaxial with the rotation axis, when the forcing frequency came into resonance with inertial eigenmodes. Strong shear layers occur near critical latitudes where the group velocity of the reflected inertial waves becomes tangential to the bounding surface of the cavity. This leads to a local thickening of the Ekman boundary layer and the generation of zonal flow, similarly to the librational-driven flows shown in Figure 8 (a, b). These critical latitudes are indicated by short white lines in Figure 8 (c). The location of the shear layers moves with the critical latitudes, which depends on the forcing frequency. The strength and width of the shear layers depend strongly on the Ekman number, which in turn is reflected in the dependence of maximum azimuthal flow as  $\sim e_a^2 E^{-\zeta}$ , where  $e_a^2$  scales the forcing amplitude and the exponent  $\zeta$  ranges from 1/10 to 3/10 in recent studies [100, 102].

Figure 8 (d) shows that strong axially-aligned zonal shear structures also form in precessionally-driven flows [92]. The two bright banded structures situated away from the rotation axis form where the inertial modes' conical shear layers are tangent to the surface of the ellipsoidal cavity. These shear layers are aligned with the total rotation vector, that includes the rotation of the container as well as the angular rotation around the precession axis.

The Figure 8 flows demonstrate that orbitally-forced flows can generate banded zonal flows. However, it has yet to be shown unambiguously that these orbitally-driven zonal flows develop robustly in the strongly turbulent, zonostrophic regime.

### 6.3. Barotropic jet flows with random forcing

The previous two subsections focus on zonal flows emergence due to global scale wave forcing. Another method, which allows a somewhat better control of the location, scale and intensity of the forcing, consists in applying a mechanical forcing, provided that it does not directly force the mean flow. Electromagnetic forcing was used to study barotropic jet formation. The working fluid is a homogeneous electrolyte through which an electric current is passed in the presence of arrays of permanent magnets, leading to the formation of vortex-like flow structures resulting from the pattern of Lorentz forces. For a recent review, the reader is referred to [103]. Another approach consists in performing an eddy-forcing using sinks and sources of fluid [15, 36, 49, 52, 104] (see also the review by [105]). In this section, we focus on updating recent progress made towards reaching a zonostrophic regime experimentally. Two experiments were recently built in

Marseille in which zonal jets spontaneously emerge from a mechanically-forced turbulent flow in a rapidly rotating water tank [33, 38, 39]. In these experiments, the fast rotation (75 revolutions per minute) of a 1 m-diameter tank with a deep water height allows to reach higher zonostrophy index, lower Ekman number and higher Reynolds number than previous experiments (see also Figure 1).

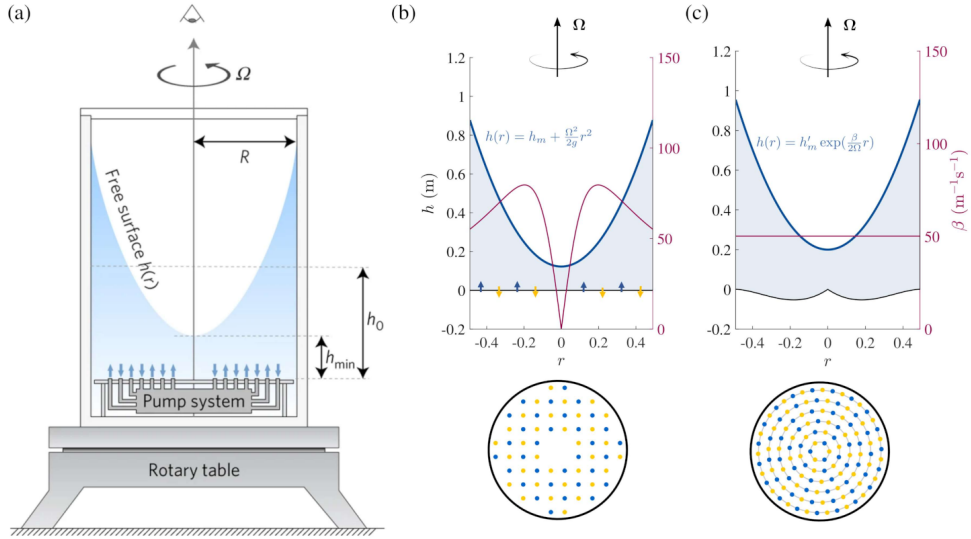


**Figure 9.** (a) Schematic section through the apparatus used by [33, 38, 39] to obtain a zonostrophic multiple-jet flow in a rapidly rotating, homogeneous fluid. The tank has a radius  $R = 0.5$  m and is rotated at  $\Omega = 7.85$  rad  $\text{s}^{-1}$  with a free surface which becomes strongly distorted into a paraboloid by centrifugal forces. Relative motions were driven by a network of inlet and outlet tubes to drive a turbulent flow. Material from [38], Macmillan Publishers Ltd: © 2017. (b,c) Free surface height (blue curve), topographic  $\beta$ -effect (purple curve) and forcing pattern in the experiments of [38] (b) and [39] (c).

Figure 9(a) shows a sideview schematic of the experimental set up used in [38, 39]. Fast rotation led to a very strong centrifugal distortion of the upper free surface into an extreme paraboloid, with the depth varying from 20 cm on the rotation axis to  $\sim 90$  cm near the periphery. This greatly curved (e.g.,  $\beta_1 \approx 3.3$ ), free-surface paraboloidal fluid layer geometry is a necessary design requirement in order to reach the zonostrophic regime in which  $R_\beta^s \gtrsim 2.5$ . The large deflection of the free surface leads to large values of  $\beta_T \approx 70$  (m.s) $^{-1}$ , due both to the high values of  $\Omega$  and due to the large value of the topographic stretching ( $h^{-1} \partial h / \partial s$ ). The free surface also greatly lowers the effects of Ekman drag which is then only present due to Ekman pumping at the bottom no-slip boundary. This is in addition to the rapid rotation rate that generates a low Ekman number,  $E \approx 10^{-7}$ . For an approximately fixed value of the forced flows, these high  $\beta_T$  and  $E^{-1}$  values are what allow for large  $R_\beta$  per (15).

As sketched in Figure 9 (b), in the first version of the experiment [38], the forcing consisted in 64 sources and sinks distributed on a Cartesian array, and the bottom of the tank was flat, resulting in a spatially varying  $\beta$ -effect. The container employed in [38] was made of polyethylene, which is not transparent. This disallowed for the passage of a horizontal light sheet through the fluid layer,



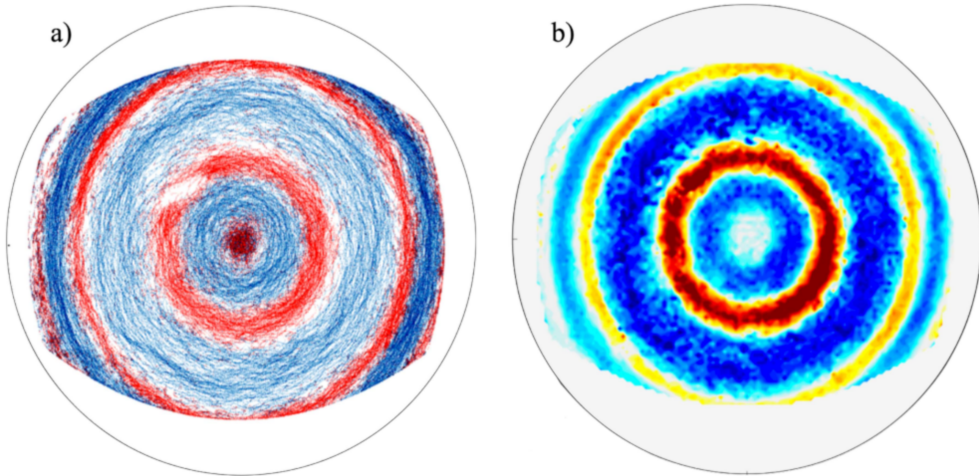


**Figure 10.** Surface floater velocity measurements from the free surface paraboloidal experiment of [38] in the zonostrophic regime. (a) Lagrangian particle tracks with path coloration given by prograde (red) and retrograde (blue) azimuthal velocity. (b) Eulerian mean azimuthal velocities,  $u_\phi(s, \phi)$ . Both panels reveal the existence of strongly coherent zonal jet flows in the zonostrophic turbulence regime ( $R_\beta^s \gtrsim 2.5$ ). Material from [38], Macmillan Publishers Ltd: © 2017.

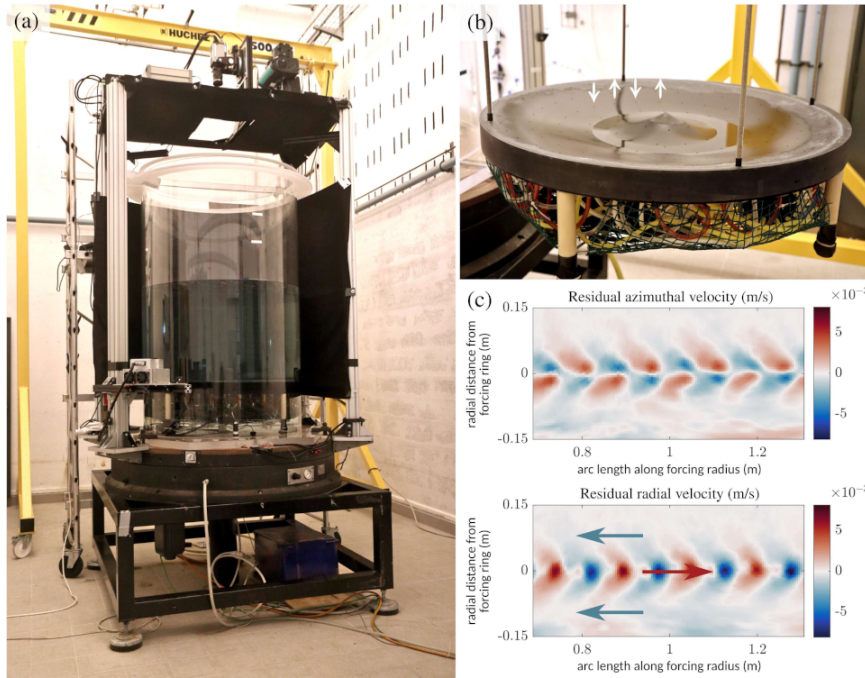
as required for standard particle image velocimetry techniques. Instead, [38] put small floating particles atop the free surface and employed Lagrangian tracking freeware [106] to generate 4900 particle tracks over the course of 5350 rotations of the tank at 75 rpm experiment.

Figure 10(a) shows these particle tracks with their local color denoting prograde particle motions in red and retrograde particle motions in blue. The formation of long period, coherent, strongly anisotropic jets is observed in the coloration pattern of the tracks.

Figure 10(b) shows the Eulerian mean azimuthal velocities, acquired by binning the Lagrangian particle tracking data that passes through a given areal region. The data shows that these flows are in the geostrophic turbulence regime, with high characteristic Reynolds numbers of order  $Re \simeq 3 \times 10^4$  and low Rossby numbers of order  $Ro \simeq 7 \times 10^{-3}$ . Further, the velocity data shows that the radial extent of the jets is well approximated by the Rhines scale,  $k_R^{-1}$ .

The particle tracking data of Cabanes et al. [38], in combination with a three-dimensional direct numerical simulation, showed that the turbulent flow exhibited kinetic energy spectra in agreement with theoretical predictions [25, 26, 107] and Jupiter observations [56]. The Rhines and transitional wavenumbers in the numerical simulation appeared to be well separated with  $R_\beta^s \approx 3.7$  calculated using using their spectral prefactor  $(C_Z/C_K)^{3/10} \sim 0.7$  in (16). If, for the sake of comparison, we use the prefactor  $(C_Z/C_K)^{3/10} \approx 0.5$  used in Figure 1, this leads to  $R_\beta^s \approx 2.6$ , which is still above the zonostrophy threshold estimated in [26, 31]. However, the sensitivity of the calculated values of  $C_Z$  and  $C_K$  calls into question the robustness of any regime boundaries defined solely in terms of  $R_\beta^s$  value. Irregardless, the agreement found in [38] between lab, computation and theory confirms the zonostrophic character of the flow in the single experiment investigated.

The primary goal of the first experimental study [38] was to generate unambiguous, multiple zonostrophic jet flows in a laboratory setting. The aim of the second study was to delve further into the generation mechanism and the long-term zonostrophic dynamics of these jet flows [33, 39]. To achieve this, an optically-clear acrylic tank was employed in [39] to allow for time-resolved



**Figure 11.** (a) Global view of the experimental setup of [39]. A laser attached on the side is used to illuminate the fluid on a horizontal sheet and perform PIV. (b) Bottom plate used to perform the source/sink forcing. Submersible pumps and tubes are attached below the plates. (c) Azimuthal and radial components of the residual velocity measured at the very beginning of an experiment. We show here an unwrapped section (from polar to cartesian) of the field of view, zoomed onto 8 sources and sinks of a forcing ring. The chevron-like pattern is indicative of Rossby waves radiated by the forcing. The red/blue arrows indicate the direction in which the zonal flow is accelerated (prograde/retrograde). Figure adapted from [39] (2021) with permission from © Cambridge University Press.

particle image velocimetry (PIV) measurements (see Figure 11(a)). Further, the bottom of the tank was curved to achieve a uniform topographic  $\beta$ -effect over the whole domain (see Figure 9(c) and a picture of the bottom plate on Figure 11(b)). This was done to allow a more straightforward comparison with theories developed in the  $\beta$ -plane framework. To achieve a better scale separation between the forcing and the jets, the forcing scale was reduced by a factor two by increasing the number of inlets/outlets from 64 to 128. Further, the inlets/outlets were distributed on a polar array and 6 submersible pumps controlled independently each one of the 6 forcing rings, allowing a precise control of the forcing amplitude with radius (Figures 9(c) and 11(b)). In these experiments, the – homogeneous – topographic  $\beta$ -effect is of about  $50 \text{ m}^{-1} \text{ s}^{-1}$ , the Ekman number  $E \sim 3 \times 10^{-7}$  and the root-mean-squared velocities could reached a few  $\text{cm s}^{-1}$ , leading to Reynolds numbers from  $5 \times 10^3$  to  $2 \times 10^4$  [33].

This second experimental set-up demonstrated that despite the strongly turbulent nature of the experiments, zonal jets emergence and non-linear equilibration are controlled by the transport and deposition of momentum by Rossby waves [39]. At low forcing amplitude, prograde jets were observed to emerge above each forcing ring, with retrograde flows in between (Figure 12), even though there were as many inlets as outlets along a given forcing ring. A careful analysis of

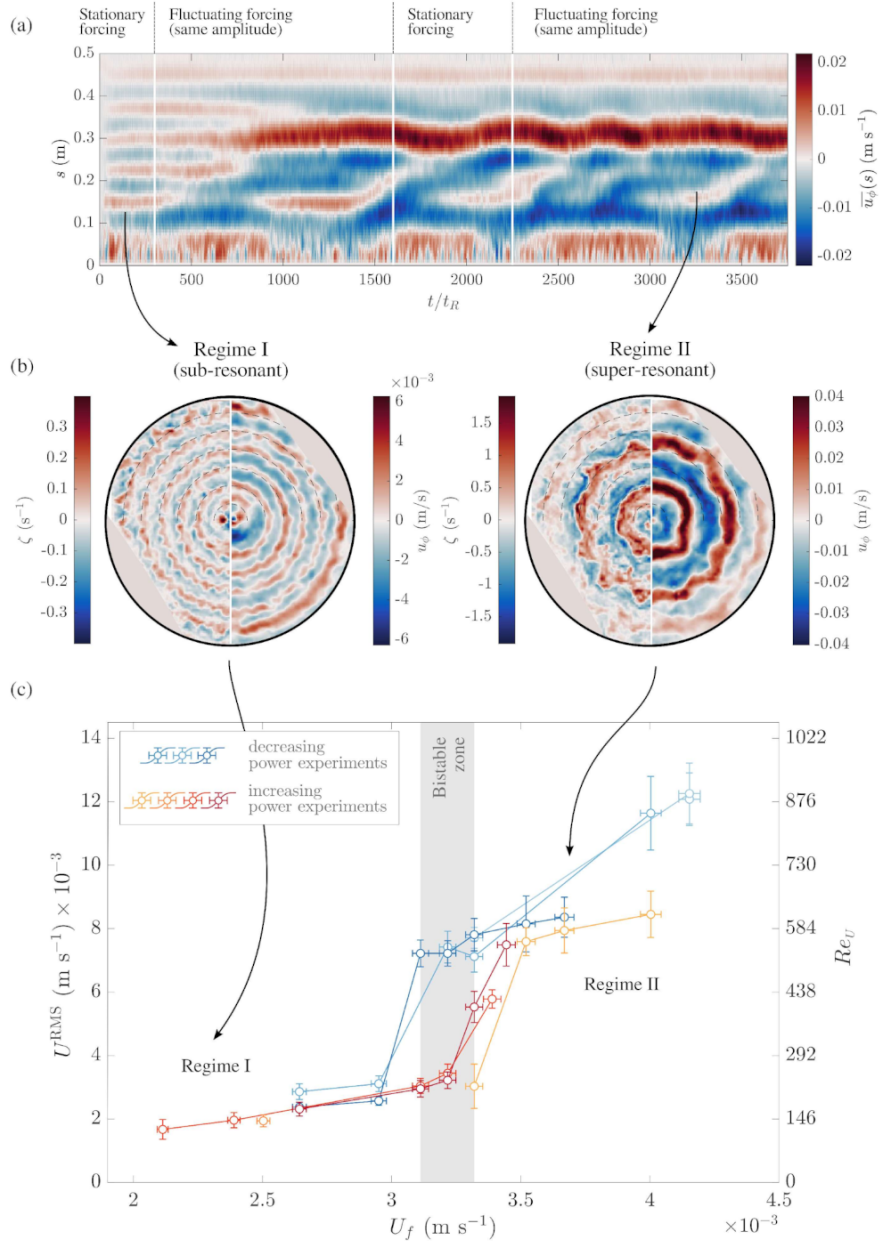


**Figure 12.** Instantaneous zonal flow in the source-sink driven experiments of [39]. (a) Space-time diagram of the zonal flow profile. The forcing amplitude is in the bistable range of panel (c), hence a transition from Regime I to Regime II is observed when “noise” is added to the forcing. (b) Instantaneous vorticity ( $\zeta$ ) and azimuthal velocity ( $u_\phi$ ) measured in an experiment at low forcing amplitude (Regime I) and at high forcing amplitude (Regime II). In the sub(super)-resonant Regime I (II), the Doppler-shifted Rossby waves phase speed is negative (positive), as resonant Rossby waves are stationary. (c) Hysteresis diagram showing the transition between the two regimes of turbulent zonal jets and associated bistability.  $U_f$  quantifies the forcing amplitude,  $\bar{u}^{\text{RMS}}$  is the root-mean-squared amplitude of the time averaged (mean) flow once in steady state, and  $Re_U$  the Reynolds number of the mean flow. Figure adapted from [39] (2021) with permission from © Cambridge University Press.

the PIV velocity fields revealed that each forcing ring radiates Rossby waves (at the forcing scale), as seen in the chevron-like patterns of Figure 11 (c). The corresponding divergence of Reynolds stresses is positive at the radius of wave emission, and negative on the flanks of the forcing region, resulting in the observed zonal flow pattern. In this first regime (called Regime I), the jets are individual and locally forced (Figure 12 (a, b)).

As the forcing amplitude was increased, a transition was observed during which the jets were seen to merge and form a set of fewer but stronger jets whose location was not correlated with the location of the mass sources and sinks, called Regime II hereafter (Figure 12 (a, b)). As demonstrated by the hysteresis diagram of Figure 12 (c), the transition comes with bistability: in some range of the forcing amplitude, both Regime I and Regime II could be obtained for the same forcing amplitude depending on the history of the system. Figure 12 (a) shows for instance an experiment at a fixed forcing amplitude in the bistable range, where adding “noise” to the forcing was enough to transition from Regime I to II. It was shown that the transition arises from a linear Rossby waves resonance due to their advection by the background zonal flow: given that Rossby waves have a retrograde phase speed, a prograde flow can make them stationary, i.e., phase-locked with the forcing, leading to their resonant amplification. This mechanism also quantitatively explains the bistability [39].

In both Regime I and II, the zonal flow profile is well correlated with the Reynolds stresses in the turbulent flow [33, 39], i.e. the zonal flow is the indirect result of correlations in the fluctuating velocities, and is never directly forced. However, while Regime I, where the jets are individual and locally forced, may be relevant for jets in the terrestrial oceans, Regime II is arguably the regime relevant for gas giants. In a follow-up study [33], the saturated turbulent and statistically steady state obtained in Regime II was analysed. Experimental PIV measurements could be used to compute kinetic energy spectra. In agreement with [38], it was shown that the measured turbulent flow shares the properties of zonostrophic turbulence relevant to the gas giants, in which the zonal flow alone contains more kinetic energy than the remaining of the flow. Spectral slopes consistent with an inverse cascade of energy were nevertheless hardly retrieved experimentally. Using two-dimensional quasi-geostrophic simulations of the experiments, [33] showed that this is due to the lack of scale separation between the forcing scale and the transitional scale. Interestingly, decreasing numerically the forcing scale allows to retrieve the theoretical slope, without influencing the final zonal flow profile. This suggests that even if the “large” experimental forcing scale prevents the development of an isotropic inverse cascade of energy, it does not limit the emergence of strong turbulent zonal jets.

Potential vorticity (PV) mixing was also investigated in strongly turbulent experiments of Regime II [33]. Despite the strength of the zonation, potential vorticity mixing is only moderate in these experiments because of the moderate zonostrophy index relatively to cases leading to strong staircasing [108]. That being said, experimental data was used to confirm that turbulent upscale energy transfer rates can be estimated by measuring a local PV mixing length, as proposed by [56] by analogy with measuring the Thorpe scale in stratified turbulence.

While these experiments were successful in indirectly forcing jets in extreme regimes, several limitations should be underlined to better understand the challenges of making more progress in this direction (see [61] for a more in-depth discussion). First, reaching a good enough scale separation between the forcing and the jets, and the jets and the experimental domain is a great challenge. Forcing the flow stronger to reach more extreme regimes means that the jets width will be larger, requiring a larger tank radius so multiple jets can fit within the fluid volume. That being said, these experiments are a clear example of the added value of the laboratory approach: a single three-dimensional direct numerical simulation at an Ekman number three times higher (e.g., [38]) requires 13 days of computation on 2048 CPU cores (650,000 CPU hours) in order to simulate 13 minutes of an experiment (1000 rotation periods). It is thus clear that numerical

systematic studies in these regimes are currently inconceivable, whereas multiple experiments can be performed, as well as experiments over very long times, allowing to study in detail the processes of jets emergence as well as their long-term nonlinear dynamics.

For instance, experiments could have a crucial role to play in investigating critical transitions between attractors. Multistability and transitions have been described in simulations of stochastically forced barotropic jets on the  $\beta$ -plane [109, 110]. For identical external parameters, several turbulent steady states with a different number or position of jets are possible and “reversals” between different jets configurations can occur. Simonnet et al. [110] observed transitions over time scales of about  $10^5$  or even  $10^6$  turnover times. Although multistability was reported in the experiments of Lemasquerier et al. [33], spontaneous transitions were not observed despite running experiments over 8 hours, corresponding to 40,000 rotation periods (see [61, Chapter 5]). Note that this corresponds to about  $10^4$  turnover times. Hence, experiments designed to run much longer and/or with a shorter turnover time would be necessary to observe rare transition events. Note also that the forcing in [33] is idealised, performed at a unique scale and spatially fixed. This could prevent long-term dynamics such as drifting zonal jets or spontaneous transitions.

#### 6.4. Zonal jets in convection

Experiments that drive eddies using devices fixed with respect to the apparatus have some advantages in allowing close experimental control on the location, scale and intensity of the applied forcing and/or initialization of turbulent motions, from which zonal flows could emerge. However, they also impose a number of geometric constraints by construction on the flow which are not typically found in systems that occur in nature on geophysical or astrophysical scales.

Free convection at high Rayleigh number in an unstably stratified fluid provides alternative and geophysically plausible means of energizing relatively unconstrained turbulent motions, albeit initially to form complex, three-dimensional circulation patterns of a form that may be hard

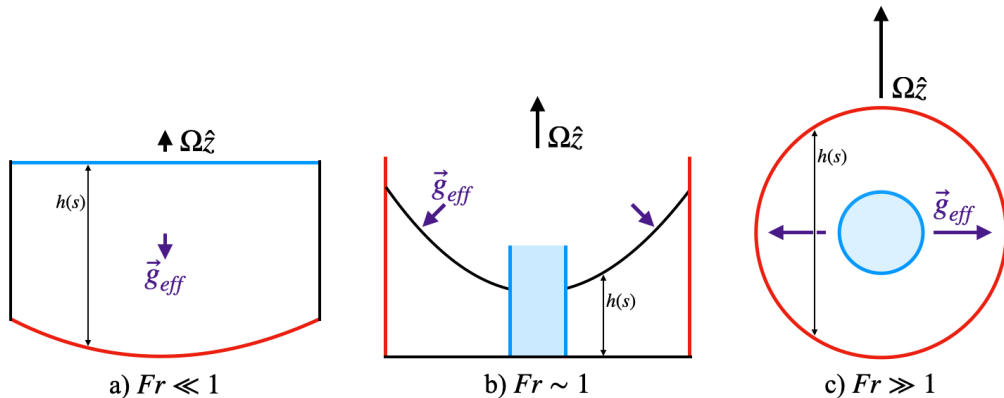


**Figure 13.** Schematic cross-sections of different experimental schemes for generating convectively-driven zonal flows. Red (blue) surfaces are actively heated (cooled). (a) Low external Froude number set-up, with axial gravity shown antiparallel to the rotation vector. (b) Moderate  $Fr$  set up, in which the free-surface equipotentials are deflected into a paraboloid. (c) Large Froude number set up in which centrifugal gravity is dominant. In cases with  $Fr \gg 1$ , such experiments must be carried out in close tanks, such as spherical shells, in order that the working fluid remain contained. In each schematic,  $h$  denotes the axial height of the fluid layer, which figures into calculations of  $\beta_T = (2\Omega/h)(\partial h/\partial s)$ .

to predict or control in detail. Even without background rotation to induce departures from isotropy, laboratory experiments have demonstrated that free convection under some circumstances can spontaneously form a rectified mean flow (e.g. [111–113]). This is associated with a spontaneous symmetry breaking of patterns of convective plumes, which become tilted in a preferred direction to result in an upward flux of horizontal momentum in a manner somewhat similar to the “moving flame” mechanism discussed above. The influence of background rotation, however, can help to organize the convection into quasi-two dimensional, vortical plume structures of a characteristic form and scale (e.g. [7, 114–124] which can seed turbulent processes that can ultimately lead to the formation of zonal flows (e.g., [43, 125]).

Differing styles of convectively-driven zonal flow experiments are carried out based on the effective gravitational acceleration, as shown in Figure 13. In laboratory settings, the effective gravity,

$$\mathbf{g}_{\text{eff}} = -g_o\hat{\mathbf{z}} + \Omega^2\mathbf{s}, \quad (25)$$

is always an admixture of vertically downward lab gravity,  $-g_o\hat{\mathbf{z}}$  (where  $g_o \simeq 9.8 \text{ m/s}^2$ ), and cylindrically-radial centrifugal acceleration,  $\Omega^2\mathbf{s}$ . The ratio of these two terms is estimated by the external Froude number,  $Fr = \Omega^2 S/g_o$  with the system’s maximum cylindrical radius  $S$  employed as the characteristic length scale.

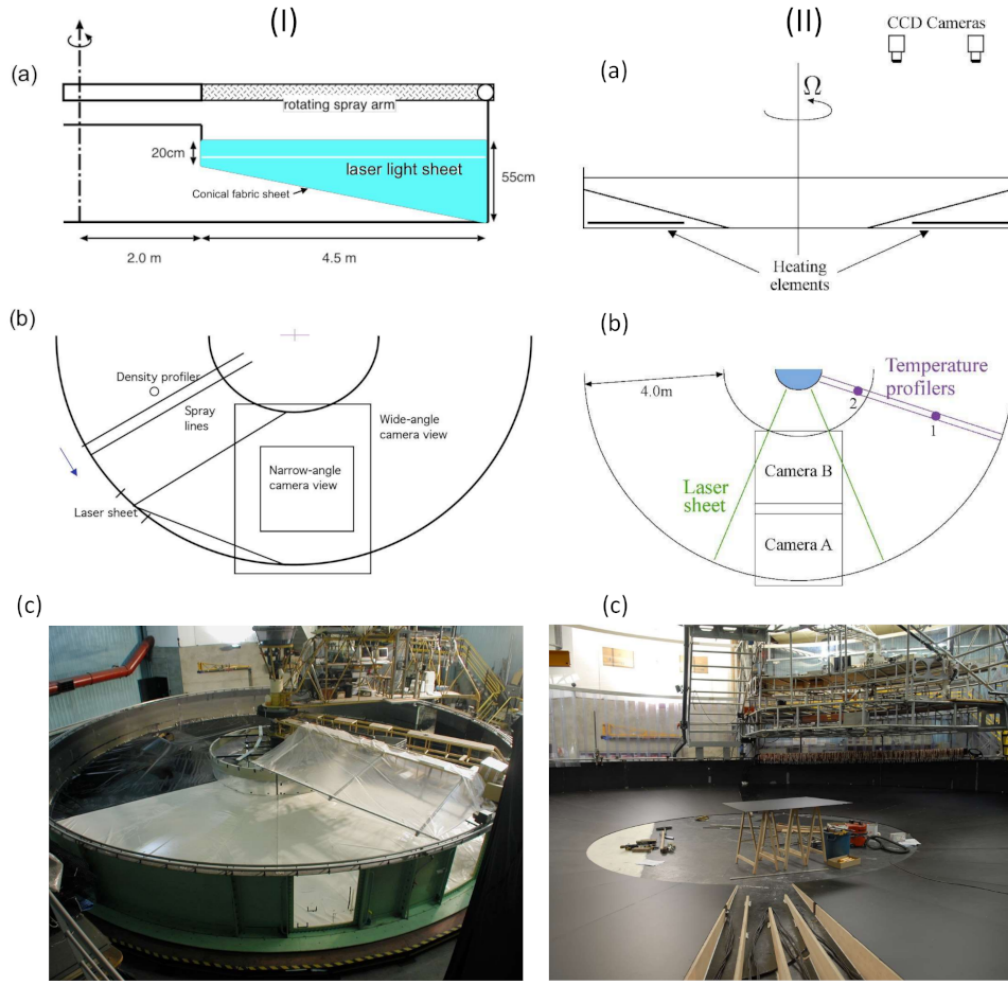
The left-hand cartoon in Figure 13(a) shows the low Froude number limit in which lab gravity is dominant. These  $Fr \ll 1$  experiments are based on “standard” upright convection. The bottom boundary here is depicted with curvature in order that  $\beta_T \neq 0$ , as is argued to be required for the formation of coherent laboratory zonal jet structures.

Figure 13(b) shows a moderate Froude, annular convection set up. In this  $Fr \sim 1$  regime, effectively gravity becomes increasingly canted away from the axial direction with increasing  $s$ . This causes the fluid’s free surface to be deflected into a paraboloid, as in to [38, 39]. The density gradients are primarily radial, being set by the thermal boundary conditions on the annular sidewalls. For a 1 m diameter tank,  $Fr = 1$  when  $\Omega = 4.4 \text{ rad/s} \simeq 40 \text{ rpm}$ .

Figure 13(c) show the rapidly rotating  $Fr \gg 1$  limit. In this end-member case, centrifugal acceleration greatly exceed  $g_o$ , and  $\mathbf{g}_{\text{eff}} \simeq \Omega^2\mathbf{s}$ . The cylindrically radial increase in outward effective gravity is qualitatively similar to the radially increasing inward spherical gravity that exists in self-gravitating uniform density spheres,  $\mathbf{g} = -(4\pi\rho G/3)\mathbf{r}$ , as adequately describes gravity in terrestrial liquid metal cores [126] and where  $\rho$  is the mass density and  $G$  is the universal gravitational constant. However, opposite to planetary gravity, the outward centrifugal acceleration requires that the inner spherical shell boundary be cooled in order to generate a convectively-unstable density profile. Note that the boundaries, which we are taking to be nearly isothermal here, are not perpendicular to  $\mathbf{g}_{\text{eff}}$  in all three systems shown in Figure 13. Thus, these convection experiments all have a nonzero component of baroclinic driving. Thermal winds will therefore always need to be deconvolved from any barotropic zonal flows that develop.

#### 6.4.1. $Fr \ll 1$ Convection Experiments

Condie and Rhines [129, 130] carried out elegant  $Fr \ll 1$  laboratory experiments that combined thermal convective forcing with background rotation and a topographic  $\beta$ -effect. In their experiments, a circular, bowl-shaped tank was filled with hot water and allowed to cool from above, inducing free convection from the upper free surface. The tank was placed on a rotating table and fluid motions near the top surface visualised and measured relative to the rotating tank. After a while, the convective motions were seen to organize themselves spontaneously into a pattern of concentric meandering jets, interspersed with closed vortices and other eddy-ing structures. The jets were interpreted by [130] as being associated with meridionally over-turning circulations arising from buoyancy forcing related to a radial gradient in depth-averaged density  $\sigma(r)$ . The jet separation distance was shown to be consistent with a scale of the order of



**Figure 14.** Schematic configurations of the 13 m diameter Coriolis Platform in Grenoble, France, as used for jet formation experiments in rotating convection [53, 127, 128]. I(a-b) Configuration I, in which convection was driven from above using a distributed spray of salt water [53]; II(a-b) Configuration II, in which thermal convection was driven from below using electrical heating beneath the sloping base [127]. I(c) and II(c) show photographic views of the Coriolis platform (I) set up for configuration I and (II) under construction for configuration II showing the network of heating cables under the sloping base.

a “deformation radius”  $L_d \sim (g[\Delta\sigma/\sigma]\bar{D})^{1/2}/f$  (where  $\bar{D}$  is the mean depth of the fluid), defined with respect to a difference in  $\sigma$  over the radial distance  $L_d$ , while the jet amplitude appeared to be of order  $U \sim fL_d$ . Such a dependence is perhaps suggestive of angular momentum conserving, or possibly a potential vorticity mixing, flow over a distance  $L_d$  (provided  $L_d \ll$  the radius  $R$  of the tank).

The mechanism considered by [129, 130] did not directly attribute the formation of the zonal jets observed to eddy processes, and likely were dominated by baroclinic, thermal wind dynamics. It was noted, however, that eddies were aligned with the zonal flows and could “contribute

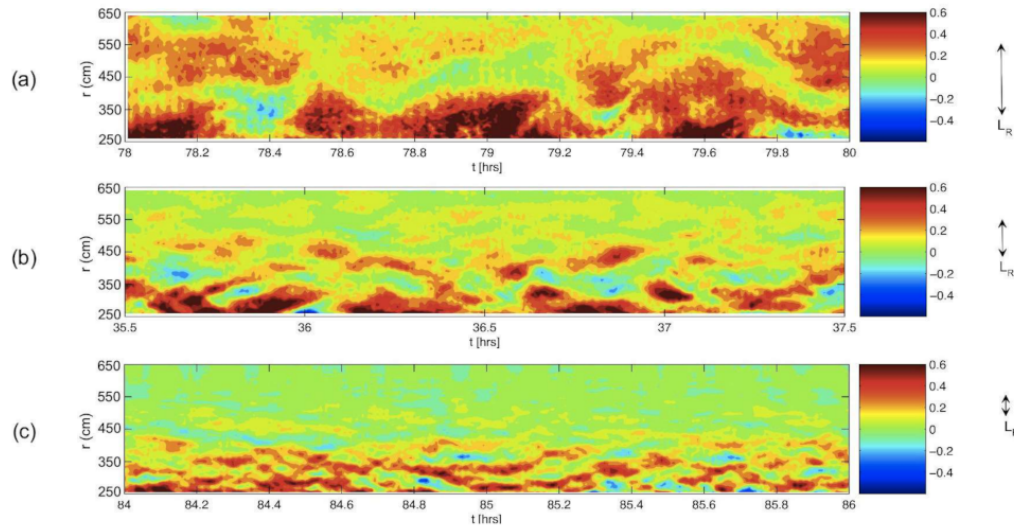


**Figure 15.** Time series of the radial structure of the azimuthal flow velocity in experiments using Configuration II of the Coriolis convection experiments [127], averaged in azimuth across the combined field of view of two overhead Cameras (see Figure 14 (II)). Results are shown for various values of rotation period  $\tau_R$  and water depth. Parameters correspond to (a)  $\tau_R = 320$  s,  $D = 0.8$  m ( $\beta^* = 43$ ), (b)  $\tau_R = 80$  s,  $D = 0.8$  m ( $\beta^* = 180$ ) and (c)  $\tau_R = 40$  s,  $D = 0.8$  m ( $\beta^* = 395$ ). Colour bars indicate the azimuthal flow velocity in  $\text{cm s}^{-1}$  and arrows indicate the Rhines lengthscale  $L_R$ .

significantly to the zonally averaged flow at certain latitudes”. The horizontal Reynolds stresses due to the wave-like meanders and vortex-like eddies were not measured directly, though appear tilted in the visualization presented in their figure 3. So it might also be the case that the zonal jets found in this experiment were also at least partially driven by eddy stresses, with the eddies themselves redistributing momentum and producing concentrated zonal jet structures fueled by convective eddies.

The role of eddies in driving the formation of zonal jets in the presence of convection was much clearer in large scale experiments carried on the 13 m diameter Coriolis platform by Read et al. [53, 127, 128]. Experiments on such a large scale enabled access to fairly extreme parameters such as the flux Rayleigh number  $Ra_F$  ( $1.5 \times 10^{10} - 6 \times 10^{13}$ ), convective Rossby number  $Ro^*$  ( $1.7 \times 10^{-3} - 4 \times 10^{-2}$ ) and Ekman number  $E$  ( $5.2 \times 10^{-6} - 5 \times 10^{-5}$ ) while keeping the Froude number quite small. The experimental configurations are shown schematically in Figure 14 as cross-sections and plan views. Two configurations were used (I and II) which both used a free surface and conically sloping lower boundary. In configuration I, convection was initiated from above by gently spraying dense, salty water onto the top surface using nozzles mounted on a radial arm [53]. For configuration II, however, convection was maintained by electrical heaters embedded under the bottom sloping boundary while the upper surface cooled to the laboratory environment [127]. In both configurations, the horizontal flow was measured using PIV with particles illuminated from one side by a powerful horizontal laser sheet.

One disadvantage of operating experiments on such a large scale was that it was impractical to view or measure the flow across the entire tank. Small arrays of cameras were therefore used to sample the flow across the full range of radii across the annular channel. This approach only



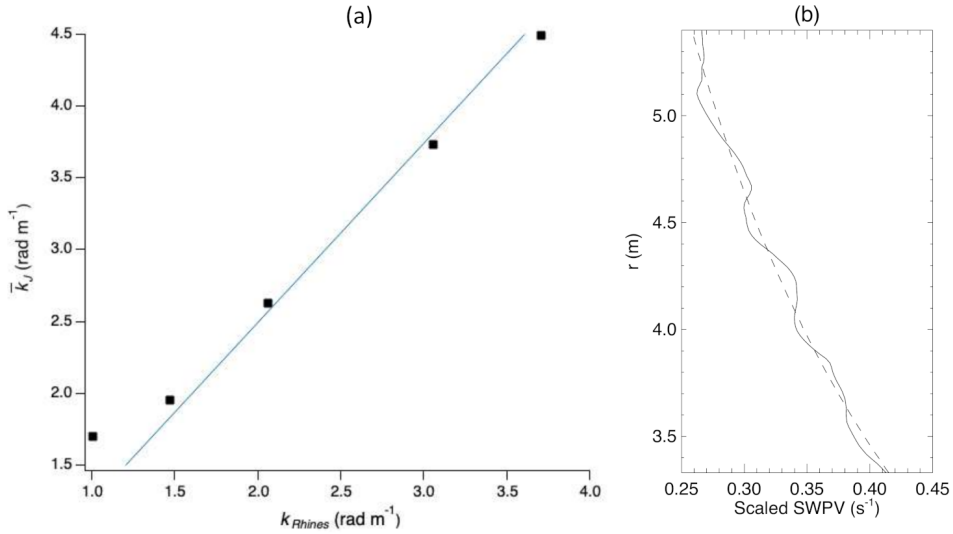


**Figure 16.** (a) Graph showing the variation of the dominant time-mean radial wavenumber  $\bar{k}_J$  of zonal jets vs estimates of the Rhines wavenumber  $k_{Rhines}$  for the thermally driven experiments illustrated in Figure 15 [127]. Straight line represents a fit to the data passing through the origin with slope  $1.25 \pm 0.04$ . (b) Radial profile of shallow water PV from 5 min time averages of zonal velocity in the salt-driven convection experiments on the Coriolis platform [53]. Solid line represents the total PV while the dashed line represents the background “planetary” component (see [53, 128] for further details).

enabled around 10% of the domain to be measured, but the spatial resolution was sufficient to resolve most of the energetic scales of motion.

As found by Condie & Rhines, the resulting convective flow was found to develop patterns of zonal jets meandering among vortices of either sign that equilibrated after a few hours of operation. Such jets were most prominent in the presence of the topographic  $\beta$ -effect due to the sloping lower boundary and the radial scale and separation of the jets was found to depend strongly on the rotation speed  $\Omega$ . Figure 15 illustrates this trend clearly for three cases in the configuration II [127], showing radius-time maps of the zonally-averaged zonal velocity at different values of  $\Omega$ . Also shown on the right of Figure 15 are estimates of the Rhines scale  $L_R$  for each case, derived using the rms horizontal eddy velocity, indicating a clear correlation between the radial wavelength of the jets and  $L_R$ .

This correlation was shown to hold over at least a factor of 4 in  $L_R$  (see Figure 16). The experiments covered a range in  $\beta_2 = \beta_T L^2 / u_{rms}$  from around 40 to 580, covering a range of jet scales from the width of the annular channel to much narrower jets with up to 5 jet pairs at the highest value of  $\beta_2$ . The strength of the jets, however, was relatively weak and scarcely different in magnitude from the non-axisymmetric eddies. This was consistent with estimates of the zonostrophy parameter  $R_\beta^s$  of between 1.5 and 1.6 which suggests all of the flows in both configurations were only marginally zonostrophic. Nevertheless, the jets were sufficiently strong to perturb the zonal mean PV profile to produce some clear staircasing, even in short-term (5 min) time averages (see Figure 16(b)).

Detailed analysis also confirmed a strong anti-correlation between the divergence of the horizontal Reynolds stress and the observed acceleration of the zonal jet flow, indicating a clear role for the eddies in generating and maintaining the latter. The analysis of Read et al. [53] went

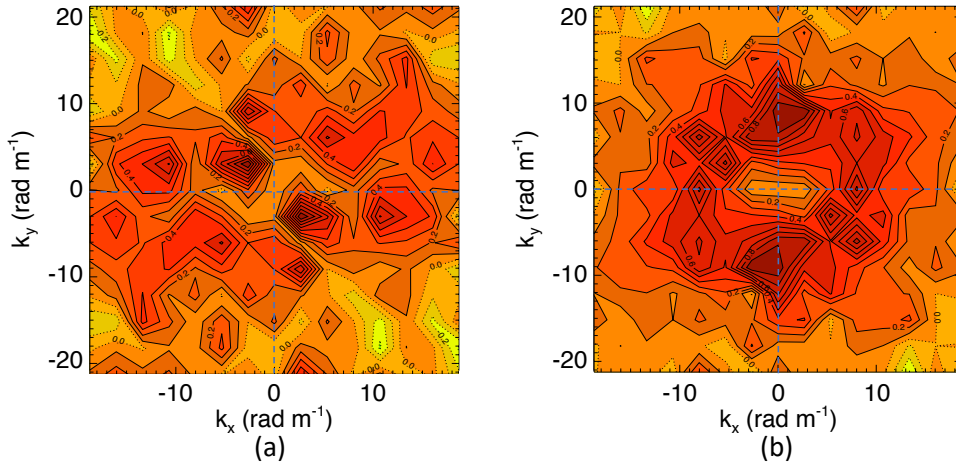


**Figure 17.** Normalized spectral energy transfer functions for two cases of salt-driven convection on the Coriolis Platform [53, 128]: (a) flat bottom (weak  $\beta$ -effect) and (b) sloping bottom with full  $\beta$ -effect, both at rotation periods of 40s. Functions were computed from sequences of vorticity fields obtained from narrow angle camera images, and integrated over triads in wavenumber that include at least one component with  $|\mathbf{k}| \geq$  cut-off wavenumber  $k_c \approx 20 \text{ rad m}^{-1}$ , averaging in time over approximately 40-50 rotation periods. Each field is normalized by the maximum value and contours are shown with interval 0.1 and with contours below 0.5 dashed.

even further to compute the nonlinear spectral transfer function in 2D,  $\mathcal{F}_E(\mathbf{k}|k_c)$  as a function of both radial and zonal wavenumbers. This measures the average rate of change of KE at vector wavenumber  $\mathbf{k}$  due to nonlinear, resonant wave triad interactions involving at least one component with  $|\mathbf{k}| \geq k_c$  [131]. The results (reproduced in Figure 17) show a clear tendency for KE to accumulate in modes close to  $k_x = 0$ , corresponding to zonal jets, for cases with a significant topographic  $\beta$ -effect. Without such a  $\beta$ -effect, however, this tendency is much less clear.

#### 6.4.2. $Fr \gg 1$ Convection Experiments

Busse and colleagues carried out the first  $Fr \gtrsim 1$  centrifugal convection experiments in simulating rotating convection and zonal flows in planetary settings [50]. Based on these experiments, it was argued that convection in the interior of a spherical planet could give rise to the generation of eddies and zonal flows that were coherent along axes parallel to the axis of rotation of the planet itself [132, 133]. The zonal flows were suggested to arise in association with Reynolds stresses that resulted from  $\beta_T$ -induced radial tilts in the convective vortices, leading to momentum fluxes that could drive zonal motions (e.g., [134]). This hypothesis was further investigated in a number of laboratory experiments using either hemispheric shells or a cylindrical annulus with conical end walls, all in rapid rotation [135–137]. Weakly nonlinear convection was induced in each case by maintaining the inner and outer spheres or cylinders at different temperatures in order to produce statically unstable stratification. These experiments were able to demonstrate the formation of fields of axially-aligned convective eddies, all roughly parallel with the rotation axis, accompanied by zonal motions, although the experiments used mostly qualitative visualisations.

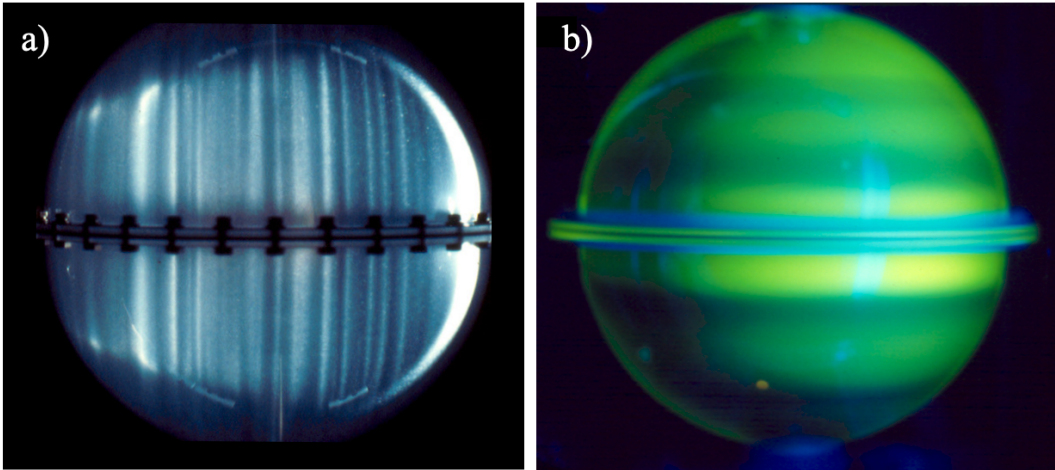


**Figure 18.** (a) Kalliroscope snapshot visualization of axially-aligned  $Ro \ll 1$  convective flow structures in a water-filled, rotating, spherical shell between spheres of radius 5 cm and 15 cm respectively at  $Ra \approx 50 Ra_c$ ,  $E = 2.5 \times 10^{-6}$  and  $Fr = 5.4$  (b) Time-lapsed dye visualization of outer boundary zonally banded flow in a rapidly rotating spherical shell containing water with differential heating between the inner and outer sphere. Images: Peter L. Olson.

Fully nonlinear centrifugally-driven spherical shell visualization experiments were extended by Olson and colleagues [138, 139]. Figure 18(a) shows a Kalliroscope visualization on a light sheet crossing the fluid bulk of a rapidly rotating spherical shell with inner and outer radii, respectively, of 5 cm and 15 cm in radius, and water as the working fluid [138]. The Kalliroscope flakes reveals axially-aligned shear structures in the convecting fluid. The control parameters for this experiment were  $Ra \sim 50 Ra_c$  (where  $Ra_c$  is the critical Rayleigh number for the onset of convection) and  $E = 2.5 \times 10^{-6}$ , with corresponding Froude number of  $Fr \approx 5.4$  (180 rpm).

Figure 18(b) shows a time-lapsed image of fluorescein dye trapped below the outer boundary in the most rapidly rotating experiment of [139]. This case was carried out at  $Ra \gtrsim 10^2$  and  $E = 7 \times 10^{-7}$  (760 rpm), such that  $Fr \approx 9.6$ . The inner shell boundary is 76% the radius of the outer shell boundary. Clear zonal banding is seen in the time-lapsed dye pattern, with as many as nine detectable zonal bands. This suggests that if similar experiments were carried out with state-of-the-art velocimetry capabilities, zonostrophic jets would form under the most extreme conditions investigated in the  $Fr \gg 1$  spherical shell experiments of [139].

Quantitative ultrasonic Doppler velocimetry measurements in spherical shell experiments made in Grenoble, using either water (with Prandtl number 7) or gallium (with Prandtl number 0.025) as the working fluid, have since been acquired by [140, 141]. The jets form consistently on a radial length scale of order  $(\bar{U}/\beta_T)^{1/2}$  in [141], where  $\bar{U}$  is the amplitude of the mean zonal flow. From the velocimetry data, it emerged that two kinds of flow regime could be identified; one (at relatively small supercritical Rayleigh numbers  $Ra_c$ ) with rather weak, meandering zonal jets and another (with  $Ra/Ra_c > 40$ ) in which the kinetic energy of the zonal flow was dominant over the non-axisymmetric flow, in a manner that seems to anticipate the Rossby resonance effects associated with the transition to “Regime II” observed by Lemasquerier et al. [39]. The amplitude of the volume-averaged zonal flow  $\bar{U}$  was found to scale with the non-axisymmetric radial flow  $V'$  as  $\bar{U} \sim V'^{4/3}$ .

### 6.4.3. $Fr \sim 1$ Convection Experiments

A number of recent experiments have investigated zonal flows using rotating cylindrical experiments in the  $Fr \sim 1$  regime, where  $\beta_T$  is set by the paraboloidal deflection of the fluid's upper free surface (e.g., [34, 40, 55, 65, 142–144]). (The fact that the baroclinic annulus jets experiments of Smith et al. [55] are referenced in this section illuminates the diaphanous, and possibly false, curtain that separates  $Fr \sim 1$  convective flows from the baroclinically-driven annular flows discussed in the following section.)

The low  $R_\beta$ ,  $Fr \sim 1$  study of [40] simulated deep ocean convection dynamics via rotating thermal convection experiments on the topographic polar  $\beta$ -plane. Their zonestrophy index of  $R_\beta \approx 1.3$  was close to oceanic values, placing these experiments within Figure 1's transitional regime. Thus, zonal jets were not a dominant feature of the flows and were only revealed after averaging. The spacing between the jets was in good agreement with the Rhines scale.

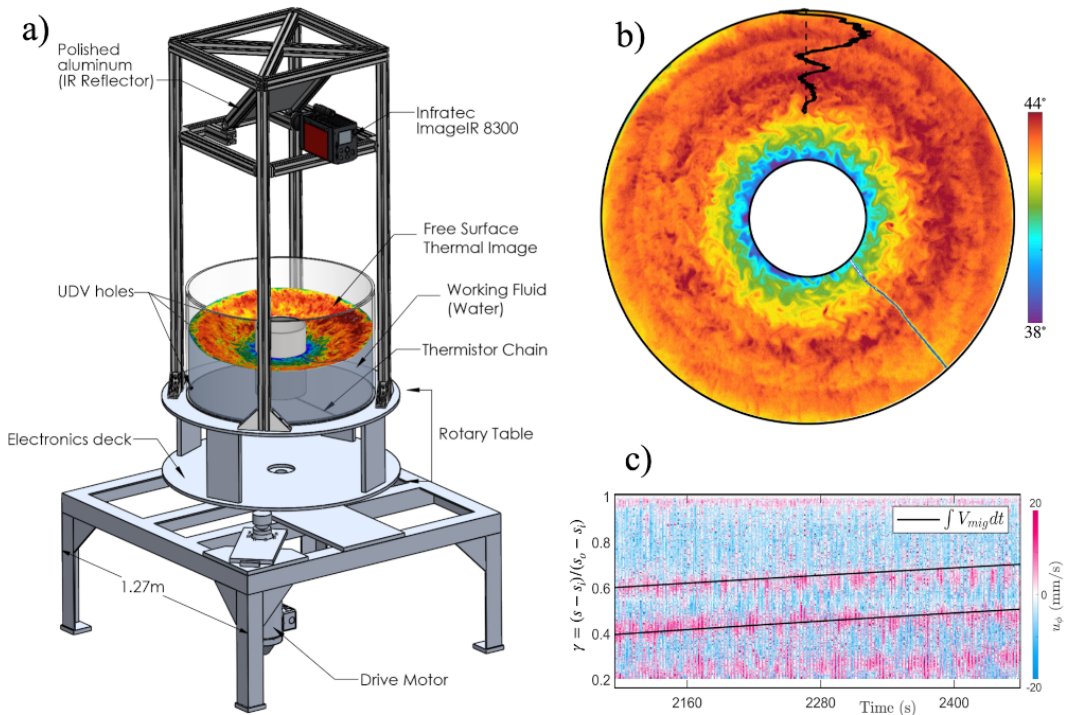


**Figure 19.** a) Schematic rendering of the “Coreaboloid” apparatus used by [34] to obtain a zonestrophic multiple-jet flow in a rapidly rotating buoyancy-driven flow. The fluid annulus has an outer (inner) radius  $R_o = 0.37$  m ( $R_i = 0.10$  m) and a free surface that becomes strongly distorted into a paraboloid by centrifugal acceleration. Thermographic free-surface overlay is from the  $\Omega = 5.24$  rad/s case (50 rpm,  $Fr = 1.0$ ). b) Thermographic top down image from the  $\Omega = 2\pi$  rad/s case (60 rpm;  $Fr = 1.5$ ). The solid black curve denotes the zonal velocity profile averaged over the last 10 minutes of the ultrasonic Doppler velocimetry data. The vertical black dashed line demarcates zero zonal velocity (aka, solid body rotation). c) Hovmuller diagram displaying ultrasonic Doppler velocimetry zonal velocity data as a function of time,  $t$ , and nondimensional cylindrical radius,  $\gamma = (s - R_i)/(R_o - R_i)$ . Solid black lines denote empirical jet migration rate predictions of Cope [145]. Figure adapted from [34]; Wiley ©2022 American Geophysical Union.

The higher  $R_\beta$ ,  $Fr \sim 1$  paraboloidal annular convection experiments of Lonner et al. [34] were carried out in similar spirit to that of Cabanes et al. [38], with the goal of generating zonostrophic laboratory jets driven by thermal buoyancy forces. Figure 19(a) shows a rendering of their “Coreaboloid” device. The tank’s inner and outer cylindrical radii are  $S_i = 10$  cm and  $S_o = 37$  cm, respectively. A thermographic snapshot of the surface temperature field from a 50 rpm experiment is overlain atop the paraboloidal free surface. The thermal buoyancy is provided by an ice bath situated within the inner cylinder. The outer wall and base are both acrylic, and thus thermally insulating. To increase the strength of the thermally-driven flows, the fluid bulk is warmed up to approximately 50° Celsius before each experiment. This increases the effective temperature drop across the fluid, but also necessitates the Coreaboloidal flows to be a complex mix of centrifugal and upright convective motions.

Rotating at 60 rpm yielded an Ekman number values of order  $E \approx 4 \times 10^{-7}$ , using the outer radius as the characteristic length scale, a peak topographic  $\beta$  value of order 1 (m.s)<sup>-1</sup>, and an estimated zonostrophy index of  $R_\beta \approx 2.7$ , corresponding to  $R_\beta^s \approx 2.67$  using the  $(C_Z/C_K)^{3/10} = 0.7$  value of [38] and  $R_\beta^s \approx 1.90$  using the  $(C_Z/C_K)^{3/10} = 0.5$  value of [26]. The zonostrophy index is smaller than the values attained in the larger volume, higher rotation rate, mechanically-driven experiments carried out in Marseilles [33, 38, 39]. The broadband buoyancy forcing in these experiments, which accurately replicates the turbulent flows that exist in natural settings, generates coherent, robust Rhines-scale jets that, agnostic to how one defines the zonostrophic regime boundaries, appear to exist in the zonostrophic regime.

Figure 19(b) shows a thermographic top view image of the free surface temperature field in the 60 rpm case from [34]. Centrifugal convective instabilities form at the inner boundary and propagate out into the bulk. The convective structures also drift in azimuth in the form of thermal Rossby waves [146]. The black solid curve denotes the time-mean azimuthal flow averaged over the last 10 minutes of the 60 rpm experiment, measured using ultrasonic Doppler velocimetry. This azimuthal velocity profile contains multiple alternating jet flows, which are in adequate agreement with Rhines length scale predictions. There is also a net retrograde flow in the Doppler data, which may be due to baroclinic thermal wind flows. Figure 19(c) displays a Hovmuller diagram of Doppler velocimetry data as a function of time and nondimensional cylindrical radius,  $\gamma = (s - S_i)/(S_o - S_i)$ . Coherent, alternating jets migrate in time, traveling outwards in radius over the range  $0.2 \lesssim \gamma \lesssim 0.7$ . The jet migration rates agree well with the empirically-derived predictions of Cope [145], based on her broad suite of two-dimensional simulations of  $\beta$ -plane turbulence.

The buoyancy-driven multiple jet flows reported in [34] imply that moderately small ( $S_o \approx 30$  cm), moderately slowly rotating ( $\Omega \approx 5$  rad/s) laboratory devices can be fabricated to study zonostrophic jet dynamics. Further, the free upper fluid surface allows for the existence of large  $\beta_T$ ,  $Re$ , and  $\tau_E$  turbulence, while simultaneously providing relatively easy access for thermographic, PIV, Lagrangian surface tracking and altimetric diagnostic methods. Significant advances in our understanding of zonostrophic fluid physics may result from well-diagnosed, broad experimental surveys of zonal jet flows in such strongly curved ( $\beta_1 \gtrsim 1$ ), free surface paraboloidal devices.

### 6.5. Zonal jets in baroclinic eddy flows

The previous Subsections 6.4.2 and 6.4.3 were mainly concerned with flows confined in rotating, annular channels with sidewall differential heating and cooling, for which the effective stratification was statically unstable, either because heating or cooling was applied at horizontal boundaries or via centrifugal accelerations modifying the direction of effective gravity. But another class of convective flows that can exhibit multiple zonal jet formation via eddy-zonal flow interactions

is represented by baroclinically unstable configurations, in which the basic flow is statically *stable* but with buoyancy sources and sinks displaced in the horizontal direction, such that isopycnal surfaces are sloped with respect to the local horizontal. The “classical” rotating annulus [147] is a type of experiment, typically with  $Fr \lesssim 1$ , which has been extensively used to investigate this configuration in the laboratory as a dynamical analogue of the baroclinically unstable, meandering jet stream in the Earth’s troposphere and in the atmospheres of other terrestrial planets. In the absence of a “planetary vorticity gradient” e.g. due to a radial gradient of depth, the basic azimuthally-symmetric flow can become baroclinically unstable at high enough values of rotation rate  $\Omega$  to traveling wave perturbations that fill the annular channel and efficiently transport heat both laterally across the channel and upwards, releasing potential energy stored in the sloping isopycnal surfaces. The resulting equilibrated flows take the form of azimuthally-traveling waves that may be either spatially symmetrical and coherent or irregular and chaotic, depending upon the values of  $\Omega$  and other control parameters. The principal dimensionless parameters that determine the flow regime observed are the Thermal Rossby number

$$\Theta = \frac{g\Delta\rho h D}{\Omega^2 L^2}, \quad (26)$$

and the Taylor number

$$\mathcal{T} = \frac{4\Omega^2 L^5}{\nu^2 D}, \quad (27)$$

where  $\nu$  is the kinematic viscosity of the fluid.  $\Theta$  and  $\mathcal{T}$  are related to  $Ra$ ,  $E$ ,  $\eta$  and  $Pr$  from Table 1 by

$$\Theta = \frac{4RaE^2\eta^2}{Pr} = \frac{4Ra}{\mathcal{T}Pr\eta^3}, \quad (28)$$

$$\mathcal{T} = E^2\eta^{-5}. \quad (29)$$

The Thermal Rossby number was originally defined as a proxy for the Burger number (see Section 2.1) based on the externally imposed *horizontal* boundary temperature contrast rather than the internally determined static stability. But it also provides an external measure of the mean Rossby number (see Table 1) provided  $\Theta \sim Ro < 1$ . The Taylor number is an alternative measure of viscous effects to the Ekman number, but also takes into account dependencies on aspect ratio  $\eta$ . The Prandtl number also plays a role, though is rather less significant than the other two (e.g. [147, 148]).

In its “classical” configuration with a flat, horizontal base and either free upper surface or flat, horizontal lid in contact with the fluid, this system has been extensively investigated in the laboratory (see [147, 148] for reviews). The dominant baroclinically unstable wave flows are found to occur with a wavelength comparable to the internal Rossby deformation radius

$$L_d^{\text{int}} = ND/f, \quad (30)$$

where  $N$  is the buoyancy frequency,  $D$  the depth of the system and  $f = 2\Omega$ , so that shorter wavelength disturbances are favored at higher values of  $\Omega$ . Without a “planetary vorticity gradient” e.g. due to a topographic gradient in either or both of the horizontal boundaries, however, the baroclinic wave flows tend to fill the annular domain in the radial direction. Amongst other things, this leads to a maximum zonal wavenumber that can remain stable and coherent, since higher wave numbers then correspond to a wave shape that has a horizontal aspect ratio (zonal:radial length scale) that is too small to be stable to Rossby wave perturbations of other wave numbers (e.g. [149, 150]), so the corresponding flow breaks up into an irregular, chaotic flow. The nonlinear interaction between the equilibrating baroclinic wave and the background zonal flow, however, will modify the latter, reducing the strength of the baroclinic jet near the centre of the channel

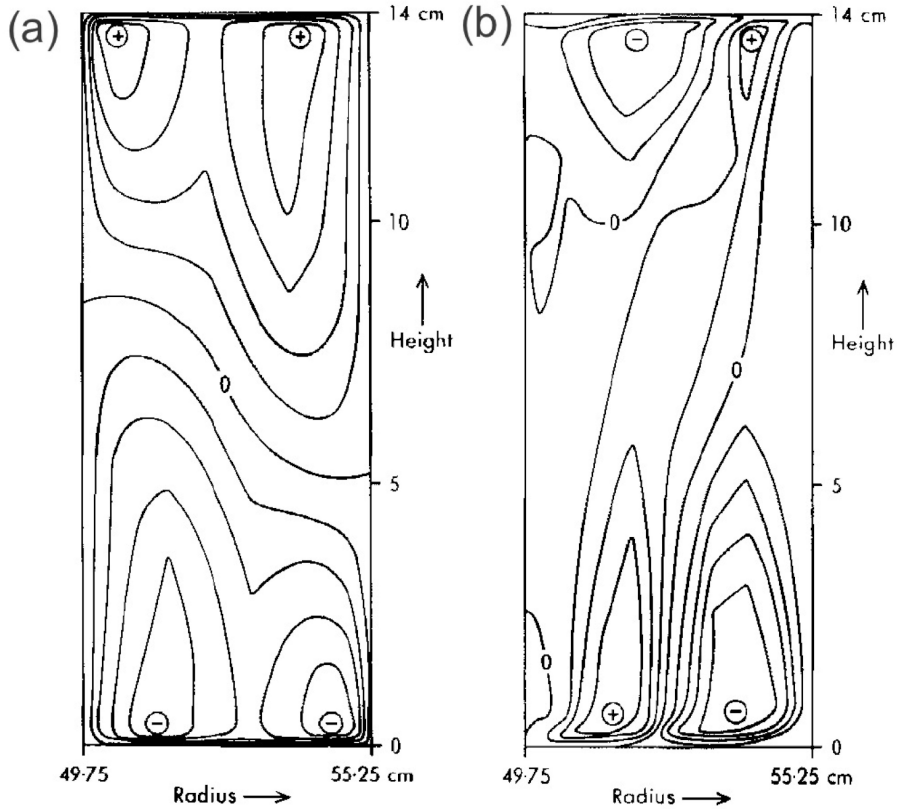


**Figure 20.** Contour maps of (a) zonal (azimuthal) flow and (b) horizontal Reynolds stress or momentum flux  $\overline{u'v'}$  in a rotating, sidewall heated/cooled annulus experiment. Fields were computed in a Boussinesq Navier–Stokes model simulation by [152] [reproduced with permission; Copyright ©1986 Royal Meteorological Society].

and effectively turning it into a baroclinic “double-jet” structure [151, 152] with azimuthal velocity maxima close to each sidewall and a local minimum of azimuthal velocity in mid-channel.

An example is illustrated in Figure 20(a) for an equilibrated steady wave flow [152]. Also shown in Figure 20(b) is the corresponding horizontal Reynolds stress field  $\overline{u'v'}$  which show the baroclinic wave acting to transfer zonal momentum into each corner jet of the appropriate sign. This indicates a strongly nonlinear interaction between the wave and its parent zonal flow, sufficient to modify the structure of the latter substantially from its form before the baroclinic wave developed.

The presence of an externally imposed “planetary vorticity gradient”, however, such as may be produced by sloping the upper and/or lower boundary to produce a radial gradient of depth across the channel, introduces a number of changes to the baroclinic wave behavior. Consistent with its effect on a barotropic wave flow, such a radial depth gradient causes the zonal propagation of baroclinic waves to become dispersive, in a manner that closely emulates the behavior of Rossby waves in the presence of a  $\beta$ -effect with a value of topographic  $\beta = \beta_T$  approximated by

$$\beta_T \approx \frac{2\Omega}{D} \frac{\partial D}{\partial r} \quad (31)$$

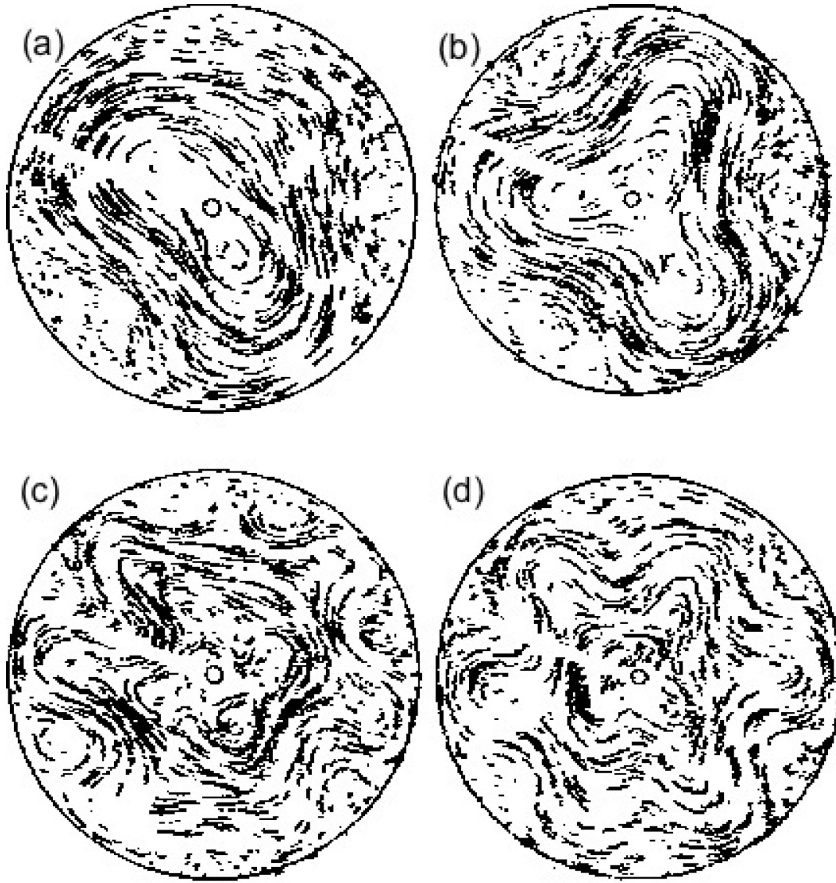


**Figure 21.** Streak images of tracer particle tracks at an upper horizontal level for baroclinic wave flows in a rotating fluid subject to internal heating and cooling at the outer sidewall, for constant heating rate and different rotation speeds  $\Omega$  (from the polar  $\beta$ -plane experiments of [154]). Low rotation rate cases (a) and (b) illustrate regular, coherent wave flows that fill the domain, but higher rotation rate cases (c) and (d) show a transition to multiple parallel wave trains and weak zonal jets.

(cf. (5) and (7) above). In addition, for large enough values of  $\beta_T$  it was found (e.g. [22] that baroclinic waves would no longer span the entire annular channel but became confined, at least initially, to a range of radii close to the inner cylinder. Further experimental investigations (e.g. [22, 153–155] have shown that this trend continues at even higher values of  $\Omega$  and  $\beta_T$  until two or more independent baroclinic wave trains are discernible at different radii, associated with the baroclinic zone within the annular channel breaking up into a banded structure.

Some clear examples of this trend are illustrated in Figure 21, which shows streak images at an upper level from a sequence of equilibrated baroclinic wave flows in an open cylinder subject to internal heating and sidewall cooling, taken from the experiments of [154]. The electrical internal heating was concentrated close to the centre of the cylinder, leading to a broad baroclinic zone spanning the entire radius of the tank (see [154] for more details). The four examples in Figure 21 illustrate changes in flow structure as  $\Omega$  was increased while keeping the heating rate constant. Relatively low rotation rate cases (a) and (b) are dominated by large, domain-filling baroclinic waves that propagate steadily around the apparatus. At a higher rotation speed, however, as in (c),



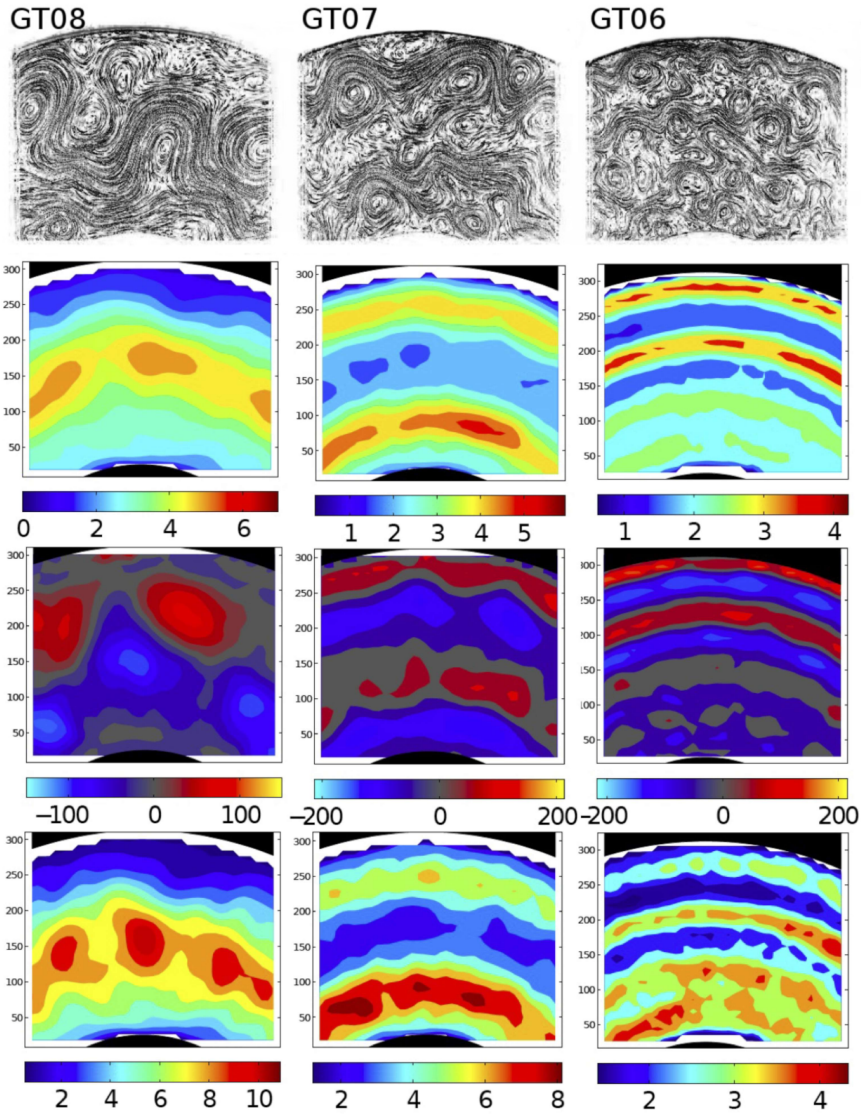


**Figure 22.** Various fields and streak images for baroclinic wave flows in a rotating fluid subject to sidewall heating and cooling, for three different rotation speeds  $\Omega$  (from the topographic  $\beta$ -plane experiments of [55]). Experiments correspond to  $(\mathcal{T}, \Theta, \beta_2)$  values of  $(9.6 \times 10^{10}, 0.061, 11.75)$  [GT08],  $(2.4 \times 10^{11}, 0.024, 43.1)$  [GT07] and  $(6.1 \times 10^{11}, 0.01, 200)$  [GT06]. Top row shows streak images of tracer particle tracks at an upper horizontal level, the second row shows time-averaged fluid speeds (in  $\text{mm s}^{-1}$ ), the third row time-averaged vorticity fields (in  $\text{s}^{-1}$ ) and the fourth time-averaged eddy kinetic energy (in  $\text{mm}^2 \text{s}^{-2}$ ). Figures reproduced from [55]; © American Meteorological Society. Used with permission.

show a higher wavenumber wave train that no longer fills the tank but is confined to a narrower band of radii, with the hint of a second wave train with a wavenumber  $m \approx 4$  nearer the centre of the tank. This becomes more clearly apparent in (d), which is taken at an even higher rotation speed experiment, within which  $m \approx 6$  is apparent near the outer cylinder but  $m \approx 3-4$  is evident

nearer the centre of the tank. This trend was found by [154] to continue to even higher rotation speeds (and weaker heating rates), such that up to three separate wave trains were discernible at three different radii. The results of [153] were broadly consistent with a Rhines scaling for the width of the baroclinic zones in their multiple wave-train regimes, and they also showed some evidence of eddies appearing at scales larger than the Rhines scale,  $L_R$ , consistent with upscale energy transfers penetrating to scales larger than  $L_R$ . In the presence of a topographic  $\beta$ -effect, spectral transfers of kinetic energy were found [155] to strengthen the azimuthally-symmetric jet-like flows, whereas with flat topography the transfers of kinetic energy were simply upscale to lower azimuthal wavenumbers. This indicates the importance of  $\beta$ -effects in favouring spectrally non-local transfers of kinetic energy into zonal jets.

More recently, Smith et al. [55] have run a series of experiments in a relatively large thermally-driven annulus experiment at the Australian National University of nearly 1 m in diameter and with a channel width of 28.75 cm. A conically-sloping bottom was used, together with a free upper surface, a mean fluid depth of 12 cm, and a range of experiments were run that explored well into the multiple wave-train regime. The results of carrying out experiments on a larger scale than hitherto were to produce flows in which the effects of viscous dissipation were significantly reduced, since horizontal wavelengths even within the multiple wave-train regime were of order 10 cm or longer, although Ekman numbers were not substantially smaller than in the smaller tanks used in the earlier studies referenced above.

Their results, however, do show some interesting advances on some of the previous studies in terms of illustrating banded jet-like features. Figure 22 shows some representative examples from their experiments in the form of streak images of upper level flows and time-averaged fields of zonal flow speeds, vorticity and eddy kinetic energy at three different rotation rates, keeping the temperature contrast across the annular channel fixed at  $\Delta T \approx 20$  K. Around a quarter of the tank could be visualized and measured at a time and the fields in Figure 22 shows such a section stretching from the inner cylinder (at the bottom of each frame) to the outer cylinder (at the top). Although instantaneous snapshots indicated highly chaotic and meandering zonal flows, the first column presents a flow with just one or two independent baroclinic jets, the second shows at least two substantial prograde jets and wave trains and the third column illustrates a flow with 3-4 separate wave trains and prograde jets. As  $\Omega$  is increased, the intensity of the meandering jets weakens as the number of jets increases, but the banded nature of the flow becomes steadily more apparent.

Figure 23 shows an example of the clear anti-correlation between the zonal mean multiple jet flow and the pattern of horizontal Reynolds stress divergence. This clearly indicates that the banded pattern of zonal flows arises in association with a strong eddy-zonal flow interaction on similar scales, with eddies tending to reinforce the multiple jet pattern and sustain it (in the zonal mean) against dissipation and other effects. The resulting jet separation was also found to scale fairly clearly with a Rhines scale, based either on the rms horizontal velocity or on the zonal mean thermal wind scale, such that  $L_{jet} \sim 5 - 8L_R$ .

A series of works by [65, 142, 143] explored a somewhat different baroclinic forcing in a domain including the pole, on a polar  $\beta$ -plane in a tank of 1.1 m in diameter. The flow is created by a coastal current of fresh water which flows along the wall of the tank on top of the layer of saline water. While the upper layer coastal current flows in the cyclonic (prograde) direction, the lower layer acquires anticyclonic (retrograde) rotation. The vertical shear in combination with the density difference is the recipe for a baroclinic instability. Baroclinic instability continuously creates meanders and filaments which protrude in a meridional direction and eventually fill the entire domain (Figure 24). The velocity in both layers was measured by a combination of altimetric, AIV, and thickness measurements, OTV. Apart from the coastal jet at the wall, at least two zonal jets can be easily identified in the interior of the domain, the direction of the flow of the

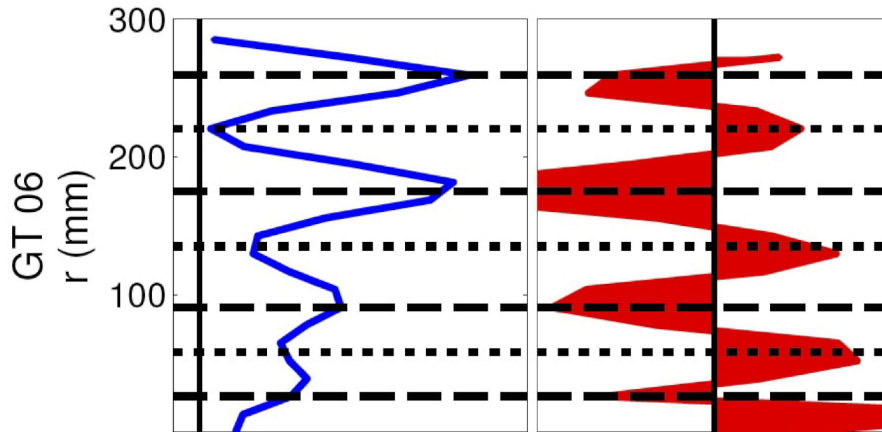


**Figure 23.** Radial profiles of azimuthal flow velocity (blue line) and Reynolds stress divergence  $1/r\partial/\partial r(r\overline{u'v'})$  (red shaded profile) for experiment GT06  $[(\mathcal{T}, \Theta, \beta_2) = (6.1 \times 10^{11}, 0.01, 200)]$ , reproduced from [55]; ©American Meteorological Society. Used with permission.

barotropic component being opposite to that of the baroclinic component. The computations of the Reynolds stress forcing shows that the jets are clearly eddy-driven.

Measurements of the meridional wavelength,  $L_{jet}$  showed its linear dependence on the baroclinic radius of deformation,  $L_{jet} = 4.4L_d$  and, at the same time, on the Rhines scale,  $L_{jet} = 0.5L_R$ . This indicates an interesting relationship between the rms velocity and the main control parameters of the flow,  $U_{rms} \propto \beta L_d^2$ .

## 7. Discussion

In the foregoing sections we have surveyed a wide range of laboratory investigations that have explored different aspects of how zonal jets can form through the action of nonlinear waves and eddies. The results of all the experiments are largely consistent with the general theory summarised in Section 3 but each experiment emphasises different components of the generalised Reynolds stress or Eliassen–Palm flux, depending upon the basic background state and experimental conditions. The range of experiments reviewed seem to indicate the following as requirements for generating substantial zonal motions from initial eddy fields in a forced-dissipative fluid flow:

- A process to generate intense eddying motions to provide a means of stirring and mixing on a scale comparable to or smaller than that of the resulting zonal motion;
- The presence of a “planetary vorticity gradient” and/or stratification to ensure that any eddies generated may be adequately wave-like and dispersive;
- A source of dissipation or “friction” on both large- and small scales, necessary to allow the flow to reach a stable equilibrium.

The first requirement is common to all of the experiments discussed. Furthermore, rotating flows that form significant eddy-driven jets generally require large, rapidly rotating domains with a strong  $\beta$ -effect, regardless of how eddies are generated. The  $\beta$ -effect is generally imposed by radially-varying topography which may be achieved either through a sloping bottom or lid or

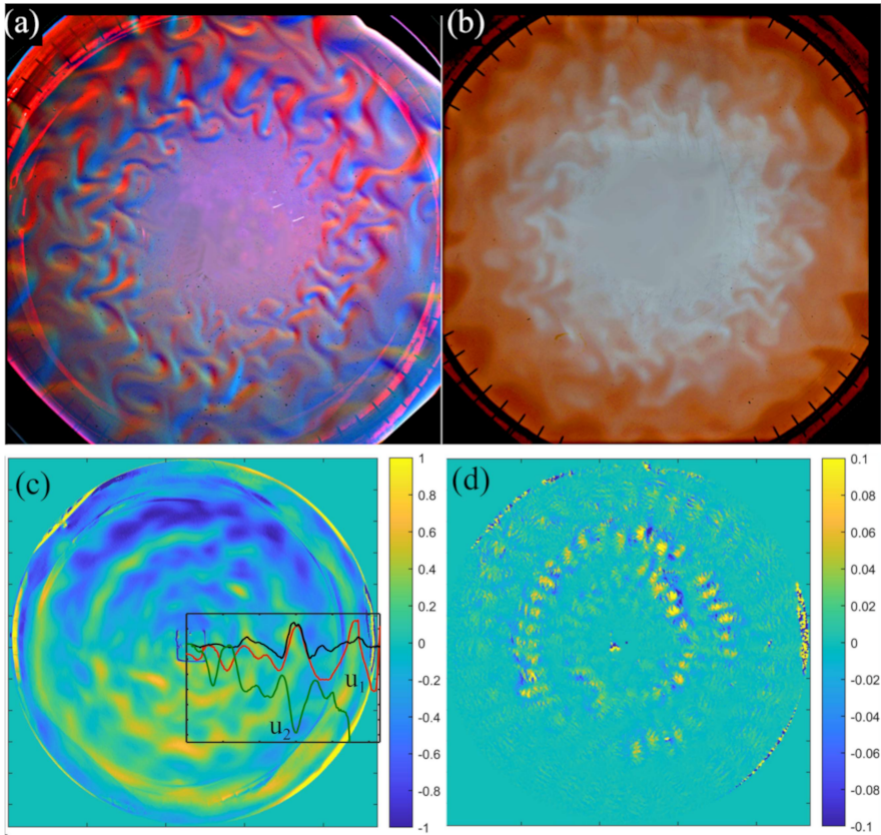


**Figure 24.** Baroclinically unstable flow on the polar  $\beta$ -plane: (a, b) Typical images of the flow obtained by AIV and OTV, respectively; (c) Barotropic azimuthal velocity measured by AIV (upper layer velocity); (d) Azimuthal component of the Reynolds stress forcing in the upper layer. Color scales show the velocity in  $\text{cm s}^{-1}$  and the forcing in  $\text{cm s}^{-2}$ . Insert in (c) shows radial profiles of the upper and lower layer velocity,  $u_1$  and  $u_2$ , and the azimuthal component of the Reynolds stress in the upper layer (black line, in arbitrary units). Figure adapted from [65].

through a centrifugally-deformed free surface. What distinguishes different types of experiment are mainly (a) in the respective roles of background rotation and stratification in determining the basic state and (b) in the way eddies or waves are generated and maintained, as discussed in next section.

### 7.1. Diversity of experiments

Much of the diversity in the experiments reported in the literature, however, derives from the eddy forcing mechanism used to energise the flow. The choice in each case largely comes from the various different planetary applications that motivate each study and, as discussed in Sections 5 and 6, may use either spatially localised or uniformly global forcing. Localised forcing is of particular interest when investigating natural flows, where the turbulence intensity is far from homogeneous in space. This can be especially significant for understanding circulation on a planetary scale which is typically non-homogeneous and anisotropic. On the other hand,

global forcing aims at studying how non-homogeneity and anisotropy may *spontaneously* emerge from homogeneous, isotropic forcing, a situation likely relevant to globally convecting planetary interiors and atmospheres.

Experiments also differ in their approach to the excitation of waves and eddies, and typically fall into one of two categories, either using fixed mechanical forcing e.g. with arrays of mass sources and sinks, or by forming basic states that spontaneously develop eddies through natural instabilities. Both approaches have both advantages and disadvantages. Natural instability forcing is in many respects more realistic when compared with processes in atmospheres, oceans or planetary interiors. But such instabilities are difficult to control experimentally and the results are consequently often difficult to interpret. Fixed mechanical forcing on the other hand is easier to control and maintain in terms of amplitude, scale and location, which can facilitate the quantitative interpretation of experimental results. But this approach is arguably less realistic compared with natural systems. So in practice both approaches have a role to play in advancing our understanding of zonal jet formation.

## 7.2. Applications

Experimental studies have been motivated by a variety of different applications to jet-like phenomena in planetary atmospheres, oceans and interiors. In many cases, experiments have enabled the elucidation of how various flow properties depend on particular parameters of the system. In stratified flows, for example, experiments have been able to verify the dependence of the strength of rectified zonal flow on wave amplitude and propagation velocity, and demonstrate the validity of a wave forcing mechanism to explain the quasi-biennial oscillation (QBO), corresponding to a nearly periodic reversal of Earth's equatorial stratospheric winds between easterlies and westerlies [80, 89].

In rotating flows, experiments have been able to demonstrate the key role of Rossby waves in the emergence and nonlinear saturation of jets, how the length scale of zonal jets is associated with the Rhines scale, at least under some conditions, and have confirmed many of the properties of the zonostrophic regime previously identified only in idealised models. Here, applications are focused towards Earth's oceans and gas giants' atmospheres and different application-driven questions motivated different experimental set-ups. For instance, localised forcing along the wall of the tank is relevant to coastal currents in the ocean (Sections 5.3), but not to the atmospheres of gas giants, where global scale forcing, unperturbed by topography, is more realistic (Sections 6.3, 6.4 and 6.5).

The distinction between deep and shallow jets has been controversial for many years in the context of the atmospheres and interiors of the gas giant planets. By exploring different experimental configurations, experiments have played an important role in clarifying the similarities and differences between such shallow and deep flows, confirming the rotational constraints that cause jet flows to align themselves along the direction parallel to the rotation axis; a property that has recently received observational support in the gravity field measurements from the Juno mission [10].

## 7.3. Key outstanding challenges

Advances in the capabilities of metrology techniques in the laboratory have ensured that experimental analogues continue to provide new insights and discoveries concerning the nature of zonal jets in turbulent flows. But while experiments have proved their worth as an avenue for such discoveries and insights which complements more traditional approaches to studying natural phenomena on geophysical scales, many challenges and outstanding questions remain for future investigation. Key challenges that deserve further attention include the following.

- The nature of, and distinction between, the friction-dominated and zonostrophic regimes of rotating, geostrophic turbulence continues to pose challenges for both models and experiments alike. Access in experiments to zonostrophic conditions has been demonstrated for values of the zonostrophic index up to around  $R_\beta^s \simeq 3$ . But accessing more extreme conditions, similar to those on the gas giant planets, is very difficult, as discussed in Section 6.3. It would be desirable, for example, to achieve a greater separation of scales between the eddy forcing and the zonal jets, but this would probably require fast rotating experiments on a much bigger scale than hitherto.
- Exploring the nature of the energy cascades that result in zonated flows also poses both theoretical and experimental challenges. Upscale energy transfer appears to be a necessary feature of zonal flow generation. But whether a more conventional homogeneous, isotropic, inverse energy cascade is necessary to the process is not yet clear. Exploration of this issue experimentally would again require maximising the scale separation between forcing and zonated scales, but expanding this substantially is difficult in practice.
- A key issue for planetary scale patterns of multiple zonal jets is how they may evolve over long timescales. Numerical simulations of planetary configurations suggest that jets may drift in latitude and the possibility of transitions and bifurcations between different kinds of jet regime may also be possible. But such investigations require very long duration experiments which will remain out of reach for high resolution numerical simulations for the foreseeable future. Experiments have an important role to play here but running experiments for a sufficiently long time relative to internal dynamical timescales is very challenging if very large experimental setups are needed to access extreme parameter regimes. Larger experimental setups with a significant scale separation between zonal jets and the size of the experimental domain also need to be developed.
- Feedback from large scales onto the small scale eddy processes can now be studied in detail, thanks to improvements in measurement techniques and the ability of some experimental configurations to run for long periods. But measurements may need to be able to keep track of the time evolution of both large scale features (evolving slowly) and very small scale waves and turbulence (evolving rapidly) to address some of the key issues.
- Interactions between highly three-dimensional eddies and deep zonal flows are still incompletely understood, though such interactions may underlie some of the complexities observed in gas giant planet atmospheres. The role of different kinds of dissipative process is another related issue where a knowledge of complex 3D structures may be required. Exploring these issues in experiments will require some ingenuity in the design of suitable configurations.
- A further open issue is the extent to which the range of rotating turbulent regimes between friction dominated and zonostrophic flows is sufficient to account for the range of circulation regimes encountered in planetary atmospheres and oceans. The Earth's atmosphere, for example, does not seem to fit comfortably into either category and exhibits an energy spectrum with some characteristic features (cf [156]) that seem anomalous compared with regimes identified from barotropic model simulations. A novel regime of rotationally controlled turbulence has been proposed [157], based on idealised model calculations, which appears to account for some of these anomalous characteristics. But this regime is yet to receive confirmation from any experimental study and its properties need further investigation.

In conclusion, therefore, the past 50 years have shown that laboratory experiments have played a clear and important role in evaluating theories and models of zonal jet formation by interactions with waves and eddies, as well as their long-term, nonlinear evolution. Further advances in measurement techniques seem likely to ensure that laboratory experiments will continue to play an important role alongside other approaches, particularly since they naturally resolve all necessary time and length scales and can be run in a systematic way over long timescales. But certain flow properties will continue to remain beyond the capabilities of direct or indirect experimental measurements, making complementary numerical simulations a highly desirable component of such investigations. For instance, modelling tools enable researchers to test the sensitivity of experimental results to some technical limitations such as the boundary conditions, e.g. to spherical geometry in place of cylindrical, as well as to variations in the nature and amplitude of forcing and dissipation.

## Acknowledgements

The authors are grateful for the constructive reviews provided by two anonymous reviewers.

## Declaration of interests

The authors do not work for, advise, own shares in, or receive funds from any organization that could benefit from this article, and have declared no affiliations other than their research organizations.

## References

- [1] P. B. Rhines, “Jets”, *Chaos* **4** (1994), pp. 313–339.
- [2] P. C. Cornillon, E. Firing, A. F. Thompson, L. M. Ivanov, I. Kamenkovich, C. E. Buckingham and Y. D. Afanasyev, “Oceans”, in *Zonal Jets* (B. Galperin and P. L. Read, eds.), Cambridge University Press, 2019, pp. 46–71.
- [3] B. Galperin and P. L. Read, *Zonal jets: Phenomenology, genesis, and physics*, Cambridge University Press, 2019.
- [4] G. K. Vallis, *Atmospheric and Oceanic Fluid Dynamics - Fundamentals and Large-Scale Circulation*, 2nd edition, Cambridge University Press, 2017.
- [5] Y. D. Afanasyev, “High-Latitude Westward Jets in the Earth’s Outer Core Due to Small-Scale Convection”, *Geophys. Res. Lett.* **45** (2018), no. 15, pp. 7454–7461.
- [6] K. Aujogue, A. Pothérat, B. Sreenivasan and F. Debray, “Experimental study of the convection in a rotating tangent cylinder”, *J. Fluid Mech.* **843** (2018), pp. 355–381.
- [7] J. Aurnou, S. Andreadis, L. Zhu and P. Olson, “Experiments on convection in Earth’s core tangent cylinder”, *Earth Planet. Sci. Lett.* **212** (2003), no. 1-2, pp. 119–134.
- [8] E. Galanti, Y. Kaspi, Y. Miguel, T. Guillot, D. Durante, P. Racioppa and L. Iess, “Saturn’s deep atmospheric flows revealed by the Cassini grand finale gravity measurements”, *Geophys. Res. Lett.* **46** (2019), no. 2, pp. 616–624.
- [9] H. Cao, J. Bloxham, R. S. Park, B. Militzer, R. K. Yadav, L. Kulowski, D. J. Stevenson and S. J. Bolton, “Strong resemblance between surface and deep zonal winds inside Jupiter revealed by high-degree gravity moments”, *Astrophys. J.* **959** (2023), no. 2, p. 78.
- [10] Y. Kaspi, E. Galanti, R. S. Park, et al., “Observational evidence for cylindrically oriented zonal flows on Jupiter”, *Nat. Astron.* **7** (2023), no. 12, pp. 1463–1472.
- [11] C. Zimmer, K. K. Khurana and M. G. Kivelson, “Subsurface oceans on Europa and Callisto: Constraints from Galileo magnetometer observations”, *Icarus* **147** (2000), no. 2, pp. 329–347.
- [12] K. M. Soderlund, “Ocean dynamics of outer solar system satellites”, *Geophys. Res. Lett.* **46** (2019), no. 15, pp. 8700–8710.
- [13] S. Bire, W. Kang, A. Ramadhan, J.-M. Campin and J. Marshall, “Exploring ocean circulation on icy moons heated from below”, *J. Geophys. Res. Planets* **127** (2022), no. 3, article no. e2021JE007025.
- [14] S. Cabanes, T. Gastine and A. Fournier, “Zonostrophic turbulence in the subsurface oceans of the Jovian and Saturnian moons”, *Icarus* **415** (2024), article no. 116047.
- [15] A. Colin de Verdière, “Mean flow generation by topographic Rossby waves”, *J. Fluid Mech.* **94** (1979), no. 1, pp. 39–64.

- [16] M. Heimpel and J. Aurnou, “Turbulent convection in rapidly rotating spherical shells: A model for equatorial and high latitude jets on Jupiter and Saturn”, *Icarus* **187** (2007), pp. 540–557.
- [17] E. R. Weeks, Y. Tian, J. S. Urbach, K. Ide, H. L. Swinney and M. Ghil, “Transitions between blocked and zonal flows in a rotating annulus with topography”, *Science* **278** (1997), no. 5343, pp. 1598–1601.
- [18] J. Herrmann and F. H. Busse, “Stationary and time dependent convection in the rotating cylindrical annulus with modulated height”, *Phys. Fluids* **10** (1998), no. 7, pp. 1611–1620.
- [19] M. A. Calkins, J. Noir, J. D. Eldredge and J. M. Aurnou, “The effects of boundary topography on convection in Earth’s core”, *Geophys. J. Int.* **189** (2012), no. 2, pp. 799–814.
- [20] U. Harlander, J. Wenzel, K. Alexandrov, Y. Wang and C. Egbers, “Simultaneous PIV and thermography measurements of partially blocked flow in a differentially heated rotating annulus”, *Exp. Fluids* **52** (2012), pp. 1077–1087.
- [21] A. P. Ingersoll and D. Pollard, “Motion in the atmospheres and interiors of Jupiter and Saturn: scale analysis, anelastic equations, barotropic stability criterion”, *Icarus* **52** (1982), pp. 62–80.
- [22] P. J. Mason, “Baroclinic waves in a container with sloping endwalls”, *Philos. Trans. R. Soc. Lond., Ser. A* **A278** (1975), pp. 397–445.
- [23] X. Q. He, A. D. Bragg, Y. L. Xiong and P. Fischer, “Turbulence and heat transfer on a rotating, heated half soap bubble”, *J. Fluid Mech.* **924** (2021), article no. A19.
- [24] L. Armi, “Hydraulic control of zonal currents on a  $\beta$ -plane”, *J. Fluid Mech.* **201** (1989), pp. 357–377.
- [25] B. Galperin, S. Sukoriansky, N. Dikovskaya, P. L. Read, Y. H. Yamazaki and R. Wordsworth, “Anisotropic turbulence and zonal jets in rotating flows with a  $\beta$ -effect”, *Nonlinear Process. Geophys.* **13** (2006), no. 1, pp. 83–98.
- [26] S. Sukoriansky, N. Dikovskaya and B. Galperin, “On the Arrest of Inverse Energy Cascade and the Rhines Scale”, *J. Atmos. Sci.* **64** (2007), pp. 3312–3327.
- [27] P. B. Rhines, “Waves and turbulence on a beta-plane”, *J. Fluid Mech.* **69** (1975), pp. 417–443.
- [28] G. K. Vallis and M. E. Maltrud, “Generation of Mean Flows and Jets on a Beta Plane and over Topography”, *J. Phys. Oceanogr.* **23** (1993), no. 7, pp. 1346–1362.
- [29] J. O’Donnell and P. F. Linden, “Free-surface effects on the spin-up of fluid in a rotating cylinder”, *J. Fluid Mech.* **232** (1991), pp. 439–453.
- [30] J. M. Aurnou, V. Bertin, A. M. Grannan, S. Horn and T. Vogt, “Rotating thermal convection in liquid gallium: multi-modal flow, absent steady columns”, *J. Fluid Mech.* **846** (2018), pp. 846–876.
- [31] B. Galperin, S. Sukoriansky and N. Dikovskaya, “Geophysical flows with anisotropic turbulence and dispersive waves: flows with a  $\beta$ -effect”, *Ocean Dynamics* **60** (2010), pp. 427–441.
- [32] A. E. Gill, *Atmosphere-Ocean Dynamics*, Academic Press Inc., 1982.
- [33] D. Lemasquerier, B. Favier and M. Le Bars, “Zonal jets experiments in the gas giants’ zonal regime”, *Icarus* **390** (2023), article no. 115292.
- [34] T. L. Lonner, A. Aggarwal and J. M. Aurnou, “Planetary core-style rotating convective flows in paraboloidal laboratory experiments”, *J. Geophys. Res. Planets* **127** (2022), no. 10, article no. e2022JE007356.
- [35] Y. D. Afanasyev and T. E. Dowling, “Evolution of Jupiter-Style Critical Latitudes: Initial Laboratory Altimetry Results”, *J. Geophys. Res. Planets* **127** (2022), no. 5, article no. e2021JE007048.
- [36] J. Sommeria, S. D. Meyers and H. L. Swinney, “Laboratory model of a planetary eastward jet”, *Nature* **337** (1989), pp. 58–61.
- [37] M. F. Jansen, W. Kang, E. S. Kite and Y. Zeng, “Energetic constraints on ocean circulations of icy ocean worlds”, *Planet. Sci. J.* **4** (2023), no. 6, article no. 117.
- [38] S. Cabanes, J. Aurnou, B. Favier and M. Le Bars, “A laboratory model for deep-seated jets on the gas giants”, *Nat. Phys.* **13** (2017), no. 4, pp. 387–390.
- [39] D. Lemasquerier, B. Favier and M. Le Bars, “Zonal jets at the laboratory scale: hysteresis and Rossby waves resonance”, *J. Fluid Mech.* **910** (2021), article no. A18.
- [40] Y. Zhang and Y. Afanasyev, “Rotating thermal convection: surface turbulence observed with altimetry and thermal radiometry”, *Geophys. Astrophys. Fluid Dyn.* **115** (2021), no. 5-6, pp. 499–522.
- [41] J. A. Abbate and J. M. Aurnou, “Rotating convective turbulence in moderate to high Prandtl number fluids”, *Geophys. Astrophys. Fluid Dyn.* **117** (2023), pp. 397–436.
- [42] S. Su, D. Cébron, H.-C. Nataf, P. Cardin, J. Vidal, M. Solazzo and Y. Do, “Acoustic spectra of a gas-filled rotating spheroid”, *Eur. J. Mech. B Fluids* **84** (2020), pp. 302–310.
- [43] T. Vogt, S. Horn and J. M. Aurnou, “Oscillatory thermal-inertial flows in liquid metal rotating convection”, *J. Fluid Mech.* **911** (2021), A5.
- [44] M. Lesieur, *Turbulence in Fluids*, 3rd edition, Kluwer Academic Publishers, 1997.
- [45] D. G. Andrews and M. McIntyre, “Planetary waves in horizontal and vertical shear: the generalized Eliassen–Palm relation and the mean zonal acceleration”, *J. Atmos. Sci.* **33** (1976), pp. 2031–2048.
- [46] D. G. Andrews and M. McIntyre, “Generalized Eliassen–Palm and Charney–Drazin Theorems for Waves on Axisymmetric Mean Flows in Compressible Atmospheres”, *J. Atmos. Sci.* **35** (1978), pp. 175–185.
- [47] V. P. Starr, *Physics of Negative Viscosity Phenomena*, McGraw Hill: New York, 1968.



- [48] P. S. Marcus and C. Lee, “A model for eastward and westward jets in laboratory experiments and planetary atmospheres”, *Phys. Fluids* **10** (1998), no. 6, pp. 1474–1489.
- [49] J. Aubert, S. Jung and H. L. Swinney, “Observations of zonal flow created by potential vorticity mixing in a rotating fluid”, *Geophys. Res. Lett.* **29** (2002), no. 18, pp. 23-1–23-4.
- [50] F. H. Busse and C. R. Carrigan, “Laboratory simulation of thermal convection in rotating planets and stars”, *Science* **191** (1976), no. 4222, pp. 81–83.
- [51] J. A. Whitehead, “Mean flow generated by circulation on a  $\beta$ -plane: An analogy with the moving flame experiment”, *Tellus* **27** (1975), pp. 358–364.
- [52] M. J. Burin, K. J. Caspary, E. M. Edlund, et al., “Turbulence and jet-driven zonal flows: Secondary circulation in rotating fluids due to asymmetric forcing”, *Phys. Rev. E* **99** (2019), no. 2, article no. 023108.
- [53] P. L. Read, Y. H. Yamazaki, S. R. Lewis, et al., “Dynamics of convectively driven banded jets in the laboratory”, *J. Atmos. Sci.* **64** (2007), pp. 4035–4056.
- [54] Y. D. Afanasyev, S. O’Leary, P. B. Rhines and E. G. Lindahl, “On the origin of jets in the ocean”, *Geophys. Astrophys. Fluid Dyn.* **106** (2012), pp. 113–137.
- [55] C. A. Smith, K. G. Speer and R. W. Griffiths, “Multiple Zonal Jets in a Differentially Heated Rotating Annulus”, *J. Phys. Oceanogr.* **44** (2014), pp. 2273–2291.
- [56] B. Galperin, J. Hoemann, S. Espa and G. Di Nitto, “Anisotropic turbulence and Rossby waves in an easterly jet: An experimental study”, *Geophys. Res. Lett.* **41** (2014), no. 17, pp. 6237–6243.
- [57] R. A. Plumb and A. D. McEwan, “The instability of a forced standing wave in a viscous stratified fluid: A laboratory analogue of the quasi-biennial oscillation”, *J. Atmos. Sci.* **35** (1978), pp. 1827–1839.
- [58] M. Le Bars, D. Cébron and P. Le Gal, “Flows driven by libration, precession, and tides”, *Ann. Rev. Fluid Mech.* **47** (2015), pp. 163–193.
- [59] M. Raffel, C. E. Willert, F. Scarano, C. J. Kähler, S. T. Wereley and J. Kompenhans, *Particle image velocimetry: A practical guide*, Springer, 2018.
- [60] W. Thielicke and R. Sonntag, “Particle Image Velocimetry for MATLAB: Accuracy and enhanced algorithms in PIVlab”, *J. Open Res. Softw.* **9** (2021), no. 1, article no. 12.
- [61] D. Lemasquerier, *Experimental and numerical study of Jupiter’s dynamics: jets, vortices and zonal flow turbulence*, PhD thesis, Aix-Marseille Université, Marseille, France, 2021.
- [62] P. B. Rhines, E. G. Lindahl and A. J. Mendez, “Optical altimetry: A new method for observing rotating fluids with application to Rossby waves on a polar beta-plane”, *J. Fluid Mech.* **572** (2007), pp. 389–412.
- [63] Y. D. Afanasyev, P. B. Rhines and E. G. Lindahl, “Velocity and potential vorticity fields measured by altimetric imaging velocimetry in the rotating fluid”, *Exp. Fluids* **47** (2009), pp. 913–926.
- [64] Y. D. Afanasyev, “Altimetry in a GFD laboratory and flows on the polar  $\beta$ -plane”, in *Modelling Atmospheric and Oceanic Flows: Insights from Laboratory Experiments and Numerical Simulations* (T. von Larcher and P. Williams, eds.), American Geophysical Union, 2014, pp. 101–117.
- [65] A. M. Matulka and Y. D. Afanasyev, “Zonal jets in equilibrating baroclinic instability on the polar beta-plane: Experiments with altimetry”, *J. Geophys. Res. Oceans* **120** (2015), no. 9, pp. 6130–6144.
- [66] J. E. Moscoso et al., “Low-cost table-top experiments for teaching multi-scale geophysical fluid dynamics”, *Front. Mar. Sci.* **10** (2023), article no. 1192056.
- [67] M. Stern, “The Moving Flame experiment”, *Tellus* **11** (1959), no. 2, pp. 175–179.
- [68] G. Schubert and J. A. Whitehead, “Moving Flame Experiment with Liquid Mercury: Possible Implications for the Venus Atmosphere”, *Science* **163** (1969), no. 3862, pp. 71–72.
- [69] J. A. Whitehead, “Observations of rapid mean flow produced in mercury by a moving heater”, *Geophys. Astrophys. Fluid Dyn.* **3** (1972), no. 1, pp. 161–180.
- [70] H. A. Douglas, P. J. Mason and E. J. Hinch, “Motion due to a moving internal heat source”, *J. Fluid Mech.* **54** (1972), no. 3, pp. 469–480.
- [71] P. J. Gierasch, R. M. Goody, R. E. Young, et al., “The general circulation of the Venus atmosphere: an assessment”, in *Venus II: Geology, Geophysics, Atmosphere and Solar Wind Environment* (S. W. Bougher, D. M. Hunten and R. J. Phillips, eds.), University of Arizona Press, 1997, pp. 459–502.
- [72] S. S. Limaye and M. Rengel, “Atmospheric circulation and dynamics”, in *Towards Understanding the Climate of Venus: Applications of Terrestrial Models to Our Sister Planet* (L. Bengtsson, R.-M. Bonnet, D. Grinspoon, S. Koumoutsaris, S. Lebonnois and D. Titov, eds.), Springer, 2013, pp. 55–70.
- [73] A. D. McEwan, R. O. R. Y. Thompson and R. A. Plumb, “Mean flows driven by weak eddies in rotating systems”, *J. Fluid Mech.* **99** (1980), no. 3, pp. 656–672.
- [74] H. M. Stommel, “Is the South Pacific helium-3 plume dynamically active?”, *Earth Planet. Sci. Lett.* **61** (1982), pp. 63–67.
- [75] M. K. Davey and P. D. Killworth, “Flows produced by discrete sources of buoyancy”, *J. Phys. Oceanogr.* **19** (1989), pp. 1279–1290.

- [76] Y. D. Afanasyev and L. M. Ivanov, “ $\beta$ -Plume mechanism of zonal jet creation by a spatially localized forcing”, in *Zonal jets: Phenomenology, genesis, and physics* (B. Galperin and P. L. Read, eds.), Cambridge University Press, 2019, pp. 266–283.
- [77] Y. Sui and Y. D. Afanasyev, “Buoyancy storms in a zonal stream on the polar beta-plane: experiments with altimetry”, *Phys. Fluids* **25** (2013), article no. 066604.
- [78] A. G. Slavin and Y. D. Afanasyev, “Multiple zonal jets on the polar beta plane”, *Phys. Fluids* **24** (2012), pp. 113–137.
- [79] T. E. Dowling, “Jets in planetary atmospheres”, *Oxford Research Encyclopedia of Planetary Science* (2019).
- [80] B. Semin, G. Facchini, F. Pétrélis and S. Fauve, “Generation of a mean flow by an internal wave”, *Phys. Fluids* **28** (2016), article no. 096601.
- [81] M. P. Baldwin, L. J. Gray, T. J. Dunkerton, et al., “The Quasi-Biennial Oscillation”, *Rev. Geophys.* **39** (2001), pp. 179–229.
- [82] R. S. Lindzen and J. R. Holton, “A theory of the quasi-biennial oscillation”, *J. Atmos. Sci.* **25** (1968), pp. 1095–1107.
- [83] J. R. Holton and R. S. Lindzen, “An updated theory for the quasi-biennial cycle of the tropical stratosphere”, *J. Atmos. Sci.* **29** (1972), pp. 1076–1080.
- [84] S. B. Fels and R. Lindzen, “The interaction of thermally excited gravity waves with mean flows”, *Geophys. Fluid Dyn.* **6** (1974), pp. 149–191.
- [85] R. A. Plumb, “The interaction of two internal waves with the mean flow: Implications for the theory of the quasi-biennial oscillation”, *J. Atmos. Sci.* **34** (1977), pp. 1847–1858.
- [86] N. Otobe, S. Sakai, S. Yoden and M. Shiotani, “Visualization and WKB analysis of the internal gravity wave in the QBO experiment”, *Nagare: Japan Soc. Fluid Mech.* **17** (1998), no. 3.
- [87] G. Bordes, A. Venaille, S. Joubaud, P. Odier and T. Dauxois, “Experimental observation of a strong mean flow induced by internal gravity waves”, *Phys. Fluids* **24** (2012), article no. 086602.
- [88] B. Semin, N. Garroum, F. Pétrélis and S. Fauve, “Nonlinear saturation of the large scale flow in a laboratory model of the quasibiennial oscillation”, *Phys. Rev. Lett.* **121** (2018), p. 134502.
- [89] B. Semin and F. Pétrélis, “Quasi-biennial oscillation: laboratory experiments”, *Comptes Rendus. Phys.* (2024), pp. 1–25.
- [90] M. Le Bars, A. Barik, F. Burmann, D. P. Lathrop, J. Noir, N. Schaeffer and S. A. Triana, “Fluid dynamics experiments for planetary interiors”, *Surv. Geophys.* **43** (2022), no. 1, pp. 229–261.
- [91] A. Tilgner, “Zonal Wind Driven by Inertial Modes”, *Phys. Rev. Lett.* **99** (2007), no. 19, article no. 194501.
- [92] J. Noir, D. Brito, K. Aldridge and P. Cardin, “Experimental evidence of inertial waves in a precessing spheroidal cavity”, *Geophys. Res. Lett.* **28** (2001), pp. 3785–3788.
- [93] J. Noir, P. Cardin, D. Jault and J.-P. Masson, “Experimental evidence of non-linear resonance effects between retrograde precession and the tilt-over mode within a spheroid”, *Geophys. J. Int.* **154** (2003), no. 2, pp. 407–416.
- [94] F. Burmann and J. Noir, “Experimental study of the flows in a non-axisymmetric ellipsoid under precession”, *J. Fluid Mech.* **932** (2022), article no. A24.
- [95] Y. Charles, *Flows driven by librations in latitude in triaxial ellipsoids*, PhD thesis, ETH Zurich, Switzerland, 2018.
- [96] A. Sauret, D. Cébron, C. Morize and M. Le Bars, “Experimental and numerical study of mean zonal flows generated by librations of a rotating spherical cavity”, *J. Fluid Mech.* **662** (2010), pp. 260–268.
- [97] J. Noir, M. A. Calkins, M. Lasbleis, J. Cantwell and J. M. Aurnou, “Experimental study of libration-driven zonal flows in a straight cylinder”, *Phys. Earth Planet. Inter.* **182** (2010), no. 1-2, pp. 98–106.
- [98] A. M. Grannan, M. Le Bars, D. Cébron and J. M. Aurnou, “Experimental study of global-scale turbulence in a librating ellipsoid”, *Phys. Fluids* **26** (2014), no. 12, article no. 126601.
- [99] D. Lemasquerier, A. M. Grannan, J. Vidal, D. Cébron, B. Favier, M. Le Bars and J. M. Aurnou, “Libration-driven flows in ellipsoidal shells”, *J. Geophys. Res. Planets* **122** (2017), no. 9, pp. 1926–1950.
- [100] C. Morize, M. Le Bars, P. Le Gal and A. Tilgner, “Experimental Determination of Zonal Winds Driven by Tides”, *Phys. Rev. Lett.* **104** (2010), no. 21, p. 214501.
- [101] A. M. Grannan, B. Favier, M. Le Bars and J. M. Aurnou, “Tidally forced turbulence in planetary interiors”, *Geophys. J. Int.* **208** (2017), no. 3, pp. 1690–1703.
- [102] Y. Lin and J. Noir, “Libration-driven inertial waves and mean zonal flows in spherical shells”, *Geophys. Astrophys. Fluid Dyn.* **115** (2021), no. 3, pp. 258–279.
- [103] S. Espa, G. Di Nitto, B. Galperin, J. Hoemann, G. Lacorata, et al., “Zonal Jets in the Laboratory. Experiments with Electromagnetically Forced Flows”, in *Zonal Jets. Phenomenology, Genesis, and Physics*, Cambridge University Press, 2019, pp. 167–177.
- [104] J. Sommeria, S. D. Meyers and H. L. Swinney, “Experiments on vortices and Rossby waves in eastward and westward jets”, in *Nonlinear Topics in Ocean Physics* (A. R. Osborne, ed.), North-Holland: Amsterdam, 1991, pp. 227–269.
- [105] P. L. Read, “Zonal Jet Flows in the Laboratory: An Introduction”, in *Zonal Jets: Phenomenology, Genesis, and Physics* (B. Galperin and P. L. Read, eds.), Cambridge University Press, 2019, pp. 119–134.

- [106] D. H. Kelley and N. T. Ouellette, “Using particle tracking to measure flow instabilities in an undergraduate laboratory experiment”, *Am. J. Phys.* **79** (2011), no. 3, pp. 267–273.
- [107] S. Sukoriansky, B. Galperin and N. Dikovskaya, “Universal spectrum of two-dimensional turbulence on a rotating sphere and some basic features of atmospheric circulation on giant planets”, *Phys. Rev. Lett.* **89** (2002), no. 12, article no. 124501.
- [108] R. K. Scott and D. G. Dritschel, “The structure of zonal jets in geostrophic turbulence”, *J. Fluid Mech.* **711** (2012), pp. 576–598.
- [109] F. Bouchet, J. Rolland and E. Simonnet, “Rare event algorithm links transitions in turbulent flows with activated nucleations”, *Phys. Rev. Lett.* **122** (2019), no. 7, article no. 074502.
- [110] E. Simonnet, J. Rolland and F. Bouchet, “Multistability and rare spontaneous transitions in barotropic  $\beta$ -plane turbulence”, *J. Atmos. Sci.* **78** (2021), no. 6, pp. 1889–1911.
- [111] R. Krishnamurti and L. N. Howard, “Large-scale flow generation in turbulent convection”, *Proc. Natl. Acad. Sci. USA* **78** (1981), no. 4, pp. 1981–1985.
- [112] E. Brown and G. Ahlers, “Rotations and cessations of the large-scale circulation in turbulent Rayleigh–Bénard convection”, *J. Fluid Mech.* **568** (2006), pp. 351–386.
- [113] T. Vogt, S. Horn, A. M. Grannan and J. M. Aurnou, “Jump rope vortex in liquid metal convection”, *Proc. Natl. Acad. Sci. USA* **115** (2018), no. 50, pp. 12674–12679.
- [114] Y. Nakagawa and P. Frenzen, “A theoretical and experimental study of cellular convection in rotating fluids”, *Tellus* **7** (1955), no. 1, pp. 2–21.
- [115] B. M. Boubnov and G. S. Golitsyn, “Experimental study of convective structures in rotating fluids”, *J. Fluid Mech.* **167** (1986), pp. 503–531.
- [116] H. J. S. Fernando, R.-R. Chen and D. A. Boyer, “Effects of rotation on convective turbulence”, *J. Fluid Mech.* **228** (1991), pp. 513–547.
- [117] F. Zhong, R. E. Ecke and V. Steinberg, “Rotating Rayleigh–Bénard convection : asymmetric modes and vortex states”, *J. Fluid Mech.* **249** (1993), pp. 135–159.
- [118] T. Maxworthy and S. Narimousa, “Unsteady deep convection in a homogeneous rotating fluid, with Oceanographic Applications”, *J. Phys. Oceanogr.* **24** (1994), pp. 865–887.
- [119] M. J. Coates and G. N. Ivey, “On convective turbulence and the influence of rotation”, *Dyn. Atmos. Oceans* **25** (1997), pp. 217–232.
- [120] S. Sakai, “The horizontal scale of rotating convection in the geostrophic regime”, *J. Fluid Mech.* **333** (1997), pp. 85–95.
- [121] J. M. Aurnou, M. A. Calkins, J. S. Cheng, et al., “Rotating convective turbulence in Earth and planetary cores”, *Phys. Earth Planet. Inter.* **246** (2015), pp. 52–71.
- [122] J. S. Cheng, S. Stellmach, A. Ribeiro, A. Grannan, E. M. King and J. M. Aurnou, “Laboratory-numerical models of rapidly rotating convection in planetary cores”, *Geophys. J. Int.* **201** (2015), no. 1, pp. 1–17.
- [123] S. Horn and J. M. Aurnou, “Regimes of Coriolis-centrifugal convection”, *Phys. Rev. Lett.* **120** (2018), no. 20, article no. 204502.
- [124] J. S. Cheng, M. Madonia, A. J. A. Guzmán and R. P. J. Kunnen, “Laboratory exploration of heat transfer regimes in rapidly rotating turbulent convection”, *Phys. Rev. Fluids* **5** (2020), no. 11, article no. 113501.
- [125] M. Wedi, V. M. Moturi, D. Funkschilling and S. Weiss, “Experimental evidence for the boundary zonal flow in rotating Rayleigh–Bénard convection”, *J. Fluid Mech.* **939** (2022), article no. A14.
- [126] B. L. N. Kennett, “Radial Earth models revisited”, *Geophys. J. Int.* **222** (2020), no. 3, pp. 2189–2204.
- [127] P. L. Read, T. N. L. Jacoby, P. H. T. Rogberg, et al., “An experimental study of multiple zonal jet formation in rotating, thermally driven convective flows on a topographic beta-plane”, *Phys. Fluids* **27** (2015), article no. 085111.
- [128] P. L. Read, J. Sommeria and R. M. B. Young, “Convectively Driven Turbulence, Rossby Waves and Zonal Jets: Experiments on the Coriolis Platform”, in *Zonal jets: Phenomenology, genesis, and physics* (B. Galperin and P. L. Read, eds.), Cambridge University Press, 2019, pp. 135–151.
- [129] S. A. Condie and P. B. Rhines, “A convective model for the zonal jets in the atmospheres of Jupiter and Saturn”, *Nature* **367** (1994), pp. 711–713.
- [130] S. A. Condie and P. B. Rhines, “Topographic Hadley cells”, *J. Fluid Mech.* **280** (1994), pp. 349–368.
- [131] A. Chekhlov, S. A. Orszag, S. Sukoriansky, B. Galperin and I. Staroselsky, “The effect of small-scale forcing on large-scale structures in two-dimensional flows”, *Phys. D: Nonlinear Phenom.* **98** (1996), pp. 321–334.
- [132] F. H. Busse, “A simple model of convection in the Jovian atmosphere”, *Icarus* **29** (1976), no. 2, pp. 255–260.
- [133] F. H. Busse, “A model of mean zonal flows in the major planets”, *Geophys. Astrophys. Fluid Dyn.* **23** (1983), pp. 153–174.
- [134] K. Zhang, “Spiralling columnar convection in rapidly rotating spherical fluid shells”, *J. Fluid Mech.* **236** (1992), pp. 535–556.

- [135] F. H. Busse and L. L. Hood, “Differential rotation driven by convection in a rapidly rotating annulus”, *Geophys. Astrophys. Fluid Dyn.* **21** (1982), no. 1-2, pp. 59–74.
- [136] C. R. Carrigan, “An experimental and theoretical investigation of the onset of convection in rotating spherical shells”, *J. Fluid Mech.* **126** (1983), pp. 287–305.
- [137] F. H. Busse, G. Hartung, M. Jaletzky and G. Sommermann, “Experiments on thermal convection in rotating systems motivated by planetary problems”, *Dyn. Atmos. Oceans* **27** (1997), pp. 161–174.
- [138] P. Cardin and P. Olson, “Chaotic thermal convection in a rapidly rotating spherical shell: Consequences for flow in the outer core”, *Phys. Earth Planet. Inter.* **82** (1994), pp. 235–259.
- [139] J.-B. Manneville and P. Olson, “Banded Convection in Rotating Fluid Spheres and the Circulation of the Jovian Atmosphere”, *Icarus* **250** (1996), pp. 242–250.
- [140] J. Aubert, D. Brito, H.-C. Nataf, P. Cardin and J.-P. Masson, “A systematic experimental study of rapidly rotating spherical convection in water and liquid gallium”, *Phys. Earth Planet. Inter.* **128** (2001), no. 1-4, pp. 51–74.
- [141] N. Gillet, D. Brito, D. Jault and H.-C. Nataf, “Experimental and numerical studies of convection in a rapidly rotating spherical shell”, *J. Fluid Mech.* **580** (2007), pp. 83–121.
- [142] A. M. Matulka, Y. Zhang and Y. D. Afanasyev, “Complex environmental  $\beta$ -plane turbulence: laboratory experiments with altimetric imaging velocimetry”, *Nonlinear Process. Geophys.* **23** (2016), no. 1, pp. 21–29.
- [143] Y. Zhang and Y. D. Afanasyev, “Baroclinic turbulence on the polar beta-plane in the rotating tank: Down to submesoscale”, *Ocean Model.* **107** (2016), pp. 151–160.
- [144] Y. D. Afanasyev and T. E. Dowling, “Evolution of Jupiter-Style Critical Latitudes: Initial Laboratory Altimetry Results”, *J. Geophys. Res. Planets* **127** (2022), no. 5, article no. e2021JE007048.
- [145] L. Cope, *The Dynamics of Geophysical and Astrophysical Turbulence*, PhD thesis, University of Cambridge, Cambridge, United Kingdom, 2020.
- [146] F. H. Busse and A. C. Or, “Convection in a rotating cylindrical annulus: thermal Rossby waves”, *J. Fluid Mech.* **166** (1986), pp. 173–187.
- [147] R. Hide and P. J. Mason, “Sloping convection in a rotating fluid”, *Adv. Phys.* **24** (1975), pp. 47–99.
- [148] P. L. Read, E. P. Pérez, I. M. Moroz and R. M. B. Young, “General circulation of planetary atmospheres: Insights from the rotating annulus and related experiments”, in *Modelling Atmospheric and Oceanic flows: insights from laboratory experiments and numerical simulations* (T. v. Larcher and P. D. Williams, eds.), American Geophysical Union, 2014, pp. 7–44.
- [149] B. J. Hoskins, “Stability of the Rossby–Haurwitz wave”, *Q. J. R. Meteorol. Soc.* **99** (1973), pp. 723–745.
- [150] P. G. Baines, “The stability of planetary waves on a sphere”, *J. Fluid Mech.* **73** (1976), pp. 193–213.
- [151] P. Hignett, A. A. White, R. D. Carter, W. D. N. Jackson and R. M. Small, “A comparison of laboratory measurements and numerical simulations of baroclinic wave flows in a rotating cylindrical annulus”, *Q. J. R. Meteorol. Soc.* **111** (1985), pp. 131–154.
- [152] A. A. White, “Finite amplitude, steady Rossby waves and mean flows: analytical illustrations of the Charney–Drazin non-acceleration theorem”, *Q. J. R. Meteorol. Soc.* **112** (1986), pp. 749–773.
- [153] M. E. Bastin and P. L. Read, “A laboratory study of baroclinic waves and turbulence in an internally heated rotating fluid annulus with sloping endwalls”, *J. Fluid Mech.* **339** (1997), pp. 173–198.
- [154] M. E. Bastin and P. L. Read, “Experiments on the structure of baroclinic waves and zonal jets in an internally heated rotating cylinder of fluid”, *Phys. Fluids* **10** (1998), pp. 374–389.
- [155] R. D. Wordsworth, P. L. Read and Y. H. Yamazaki, “Turbulence, waves and jets in a differentially heated rotating annulus experiment”, *Phys. Fluids* **20** (2008), article no. 126602.
- [156] G. D. Nastrom and K. S. Gage, “A climatology of atmospheric wave number spectra of wind and temperature observed by commercial aircraft”, *J. Atmos. Sci.* **42** (1985), pp. 950–960.
- [157] B. Galperin and S. Sukoriansky, “Quasinnormal scale elimination theory of the anisotropic energy spectra of atmospheric and oceanic turbulence”, *Phys. Rev. Fluids* **5** (2020), article no. 063803.